2023 Doctor Dissertation

Protein assembly fabrication and evaluation utilizing laser micro-manipulation

(レーザー微細操作を駆使したタンパク質集合体の作製と評価)

Po-Wei Yi (易柏維)

Nara Institute of Science and Technology
Materials Science　Bio-Process Engineering Lab
（Main supervisor　Hosokawa Yoichiroh）

Submission Date: January. 6, 2023

INDEX

Chapter 1 Introduction

1.1 Protein assembly

Other than water, protein is the most abundant matter in the biology. Depends on the function of the protein molecules such as practical control or adjustment of the chemical process for the maintenance of our regular lives [1]. Intriguingly, the interaction among protein molecules has been investigated and discussed in terms of micro-biology, synthetic biology and cellular engineering [2]. In the case of the living organism, proteins most likely aggregate or assemble through their interaction, which depends on their intrinsic property and the condition of the environment, such as the intermolecular distance and the pH value [3]. This aggregate and assemble behavior are two sides to the same coin; on one hand, the aggregation of misfolding or disorder of the protein molecules may lead to neurodegenerative diseases such as Alzheimer's and Parkinson's diseases [4]; on the other hand, more and more evident literature points out the aggregate or assembly can be potentially beneficial to the biological function such as molecular scaffolding to memory if it is regulated appropriately by the cell [5–8].

Protein assembly, including protein crystal, is an indispensable material in bio-process engineering. Processes and methodologies for fabricating and evaluating the protein assembly are widely investigated and discussed [9]. The common application of protein assembly is protein-based materials with the property of biodegradability and biocompatible. Some proteins devoted to studying the protein-based application are well-known in the food-conservation industry for their effortless availability; for instance, silk fibroin and soy protein isolate films [10,11]. Furthermore, the plenty of application of

medical device is used of the protein-generated materials including countless advantage. Hence, understanding and the fabrication of the protein assembly is the crucial strategies in terms of the materials engineering. **Figure 1.1** shows the current employment of the protein film methods.

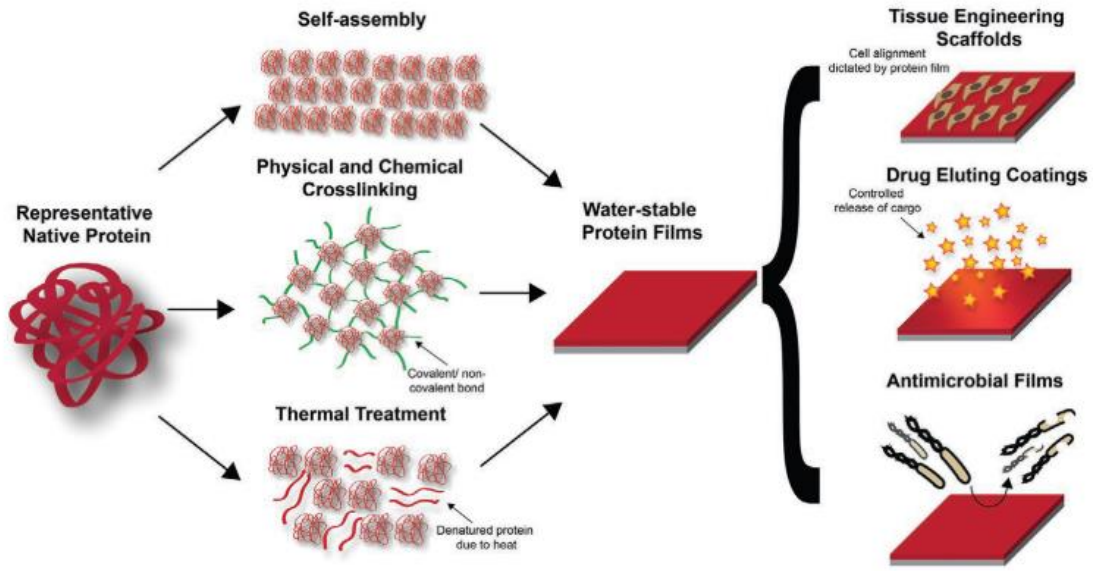

Figure 1.1 Schematic illustration of strategies of fabrication of protein films and examples of biomaterial applications. Stable protein films can be fabricated through self-assembly of proteins, physical, or chemical crosslinking, and thermal treatment from the nature protein. Applications of protein films include tissue engineering scaffolds, drug eluting coatings and antimicrobial surfaces [9].

1.2 Optical trapping

Dr. Arthur Ashkin has discovered optical trapping, also refers as optical tweezer technique in 1986, won the Nobel physics prize in 2018. He showed that radiation pressure from intense, coherent lasers could accelerate, decelerate, steer and even trap small, micron and nano-sized particles in solution without any contact. More importantly, optical trapping is compatible with various types of light microscopy, such as bright field

and fluorescence microscopy. These features have allowed optical trapping to become one of the most successful micro-manipulation tools in physics, chemistry and biology fields. For example, as shown in the **Figure 1.2** [12], a single trap configuration for studying DNA binding protein at the single protein level. One end of the DNA is attached to a glass coverslip via chemically linkage, while RNA polymerase is manipulated via an optically trapped bead. With the systematic investigation, providing detailed insight into transcription fidelity. This is one demonstration of the optical trapping application, still there are numerous cutting-edge technologies are pioneered by optical trapping.

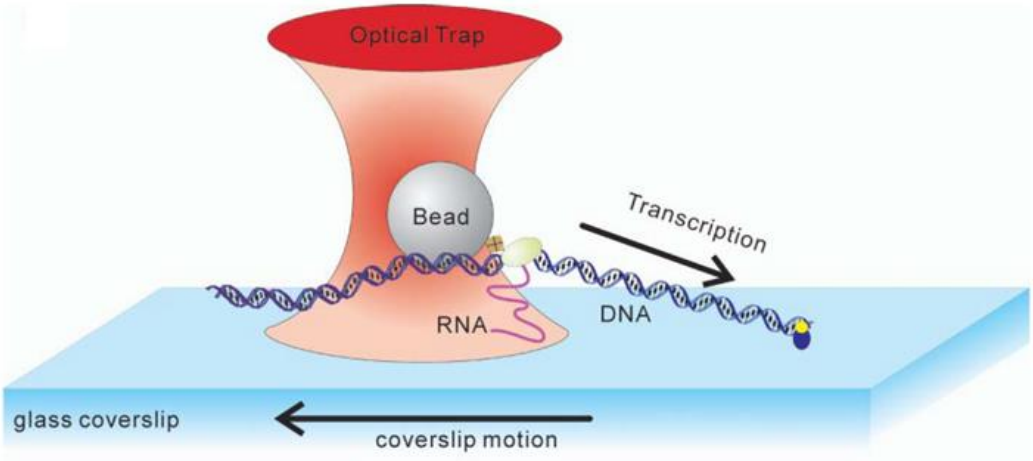

Figure 1.2 Schematic illustration of optical tweezers configurations used to study RNA polymerase. A single trap configuration is shown. One end of the DNA is attached to a glass coverslip via a digoxigenin– antidigoxigenin linkage, while RNA polymerase is attached to an optically trapped bead via an avidin–biotin bond. The bead position is maintained by stage motion to provide constant tension (typically from right to left) [13].

Optical trapping is a powerful tool as its precise spatial controllability for the manipulation of the micro- and nano-sized objects such as polymer, colloids, vesicles, aerosols, nanomaterials, viruses, living cells, and so on. In theory, light can exert radiation pressure and torque on the target due to the carried linear and angular momentum [14]. In

most cases, optical trapping exerts the optical force generated by the change of momentum, usually resulting from the tightly focused and coherent laser beam, on the targets. The resulting force can be classified by directional acceleration into two components: gradient force and scattering force. Gradient force indicates a force that always points toward the highest intensity region of the irradiation (i.e. the laser focal point) and confine the particle at the laser focus. On the other hand, scattering force is a representative as the pushing force along the beam axis, indicating the direction of light propagation. **Figure 1.3**, the motion of the particle is dominated by the relation of these two components. Therefore, a stable tapping condition is established where the gradient force exceeds the scattering force, mostly localizing the objects at the laser focal point.

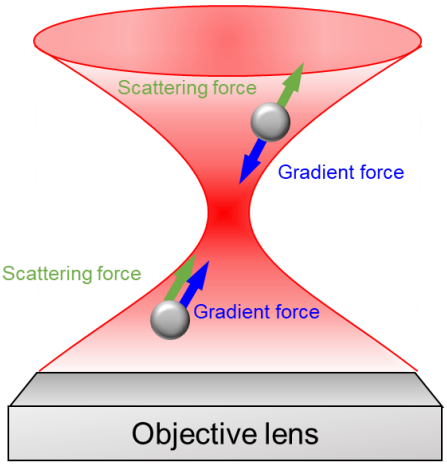

Figure 1.3 Schematic illustration of the optical trapping dividing into two force, scattering force (green arrow) and the gradient force (blue arrow). Scattering force is the pushing force along the optical axis. Gradient force is the trapping force toward the laser focal point.

According to the theoretical viewpoint of the exerted force from optical trapping, gradient force and scattering force can be interpreted by considering the scale of object as two distinct model, geometrical (ray optics) regime and the Rayleigh (dipole approximation) regime. The object whose size is much larger than the wavelength of

incident laser beam, attributed to the ray optics regime. **Figure 1.4** illustrates the concept of ray optics regime regarding to the momentum transfer due to the beam refraction. The refraction and light inflection take place, while it penetrates to the particle because of the refractive index difference between the particle and the surrounding medium. Based on the momentum conservation, the momentum change due to the refraction would generate the momentum with the exact magnitude with opposite direction. Neglecting the minor surface reflection from the particle. The generated momentum acts as the force on the particle to displace it to the laser focus as long as its refractive index is larger than the surrounding. Vice versa, the particle would be scattered away if its refractive index is smaller than the surrounding. In the case of stable trapping, the gradient force must overcome the scattering force.

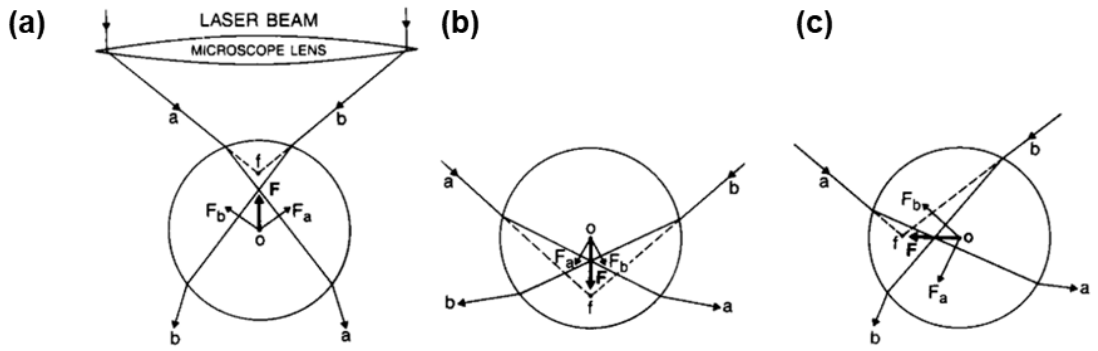

Figure 1.4 Illustration of the trapping of dielectric spheres with the particle size r (r >>λ). The refraction of a typical pair of rays a and b of the trapping beam gives forces Fa and Fb whose vector sum F is always restoring for axial and transverse displacements of the sphere from the trap focus f. Figures described that particle has the initial position O above (a), below (b) and (c) at the lateral side of the focus [15].

Regarding Rayleigh regime, the particle size is smaller than the wavelength of the incident beam such as nano particle, single atom/molecule, the acting force can be described as the Lorentz force. Considering the interaction of the electromagnetic field of

the laser beam with the object itself treated as a point dipole can express the optical force for the Rayleigh regime. The following equation can give a general expression of the optical trapping force,

$$\vec{\mathrm{F}} = \frac{\alpha}{2}\vec{\nabla}|E^2| + \alpha\frac{\partial}{\partial t}(\vec{E}\times\vec{B}) \qquad (1.1)$$

The first terms in **Equation (1.1)** represents the optical gradient force, as it is proportional to the gradient of the irradiance of the field where α represents the polarizability of the particle. This is a conservative force that results in particles with a high refractive index relative to their surroundings being pulled toward the region of maximum light intensity. In an optical tweezers, this is the focal volume of the light beam [16]. The second term in **Equation (1.1)** represents the non-conservative scattering force, which is radiation pressure force that acts to push the particle in the direction of the light propagation axis. In addition, the magnitude of the optical force acting on a particle can be maximized by choosing to use a particle with a high relative polarizability as the polarizability α can be described as the following equation,

$$\alpha = 4\pi n_m^2 \epsilon_0 r^3 \left(\frac{m^2-1}{m^2+2}\right) \qquad (1.2)$$

where r is the radius of the particle, ϵ_0 is the permittivity in vacuum, and m is the relative refractive index of the particle compared to its surrounding medium, $m = n_p/n_m$: n_p is the refractive index of the particle and n_m is the refractive index of the surrounding medium. The effects on the optical forces of changing both the particle refractive index, np, and the particle size, r, are significant. Furthermore, when the particle size is smaller, the Brownian motion (k_BT) is more un-negligible. Its condition is similar to the ray optics

regime for stabilizing the trapped particle. The gradient force must exceed the scattering force and the Brownian motion.

1.2.1 Optically evolved assembling

In the most studies, optical trapping is carried out inside the solution where a single micro particle or the assembly of nanoparticles or molecules are compacted within the laser focal point. In the past decade, our group discovered the new phenomena by shifting the laser focus from bulk solution to the solution surface or interface thereby extending the assembly of particles or molecules to the outside of the trapping laser focus. We have been devoting on deepen the knowledge of this phenomena, we call it **optically evolved assembling**.

Optically evolved assembling was firstly discovered by laser trapping of 200 nm polystyrene nanoparticles (PS NPs) at air/solution interface of the colloidal heavy water solution [17]. When plural NPs are trapped in an optical focus at the interface and form an aggregate, the trapping laser is scattered from the focus, propagates through the aggregated NPs and expands the optical trapping potential to the outside, giving a large disk-like assembly, as shown **Figure 1.5**. The assembly which is periodically arrayed by NPs is examined using the reflection microspectroscpy.

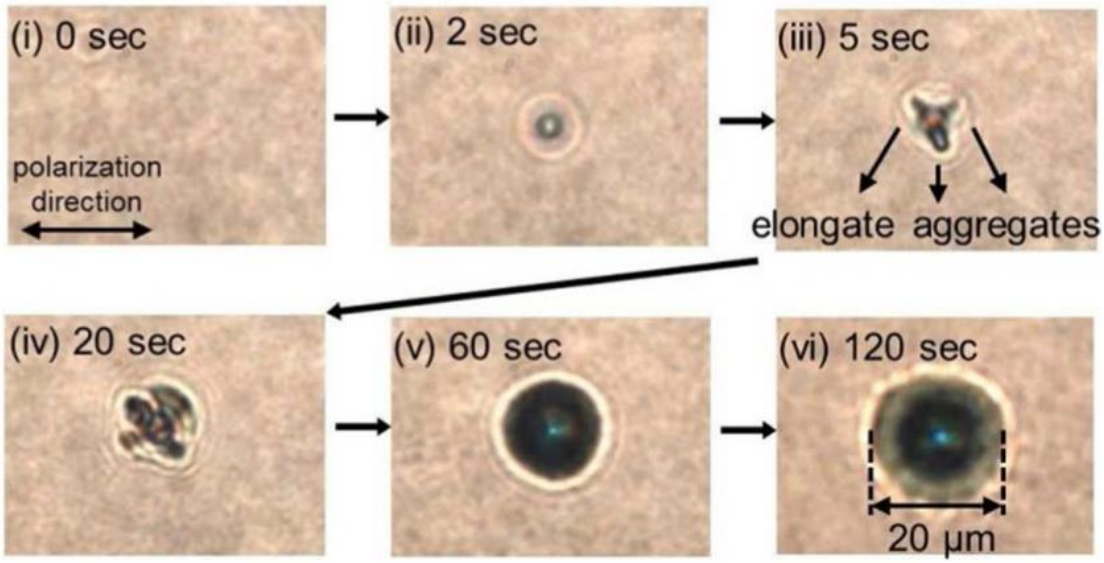

Figure 1.5 The transmission image of the optical evolved assembling for 200 nm PS over the trapping laser irradiation time course.

In the case of PS microparticles (MPs) with diameter of 1 μm at the solution surface, initially a concentric circle-like structure is prepared as an assembly, and then it is transformed to a hexagonal close packing structure by ejecting some MPs [18]. During the irradiation, the dynamical fluctuation of MPs is in the assembly, and some of them are ejected when newly coming MPs collide with the concentric circle-like assembly from the bulk solution. Eventually, the hexagonal close packing structure is formed and expanding outside from the laser focal point over time course. It was directly confirmed that the assembling, transformation, and ejection are all driven by optical force using back-scatter imaging (**Figure 1.6**).

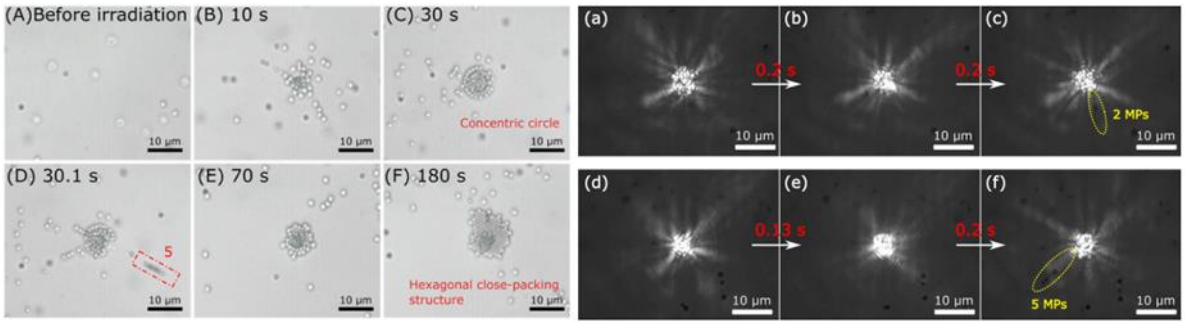

Figure 1.6 Left: Transmission image series of laser trapping induced formation of 1 μm PS at solution surface. (A) before trapping laser is turned on and (B-F) the time after trapping laser is switched on. Right: backscattering images from the transmission images without turning on the halogen lamp. The bright laser speckle pattern in the image center is the back-scattered pattern of the 1064 nm trapping laser. Among these images, 1 μm PS is recognized as the small black dot. The yellow dotted circles indicate the ejected particles in a linear manner.

In the case of molecular level, L-phenylalanine for example [19], focusing the trapping laser at the solution surface may generate the dense domain consisting of a large number of the liquid-like clusters is formed prior to the crystallization. The resultant clusters are trapped in the focal volume, and local concentration is increased nonlinearly with time. The small domain formed at the focal spot is extended to the surrounding solution due to intermolecular/cluster interactions, heat transfer, and convection. During laser irradiation into the dense domain, crystal nucleation is stochastically triggered at the focal spot (**Figure 1.7**). The dynamic and the mechanism were also established by observing that the PS particles gather to the crystal surface even without direct trapping irradiation [20] (**Figure 1.8**). The trapping dynamics in viewpoint of the propagated light possibly generates optical potential at the crystal surface, where crystal growth proceeds. Subsequently, the laser light can be propagated to further distant position through this optically induced crystal growth, leading to continuous crystal growth. Upon switching

off the laser irradiation, the crystal gradually dissolved and became smaller because of the unsaturation condition.

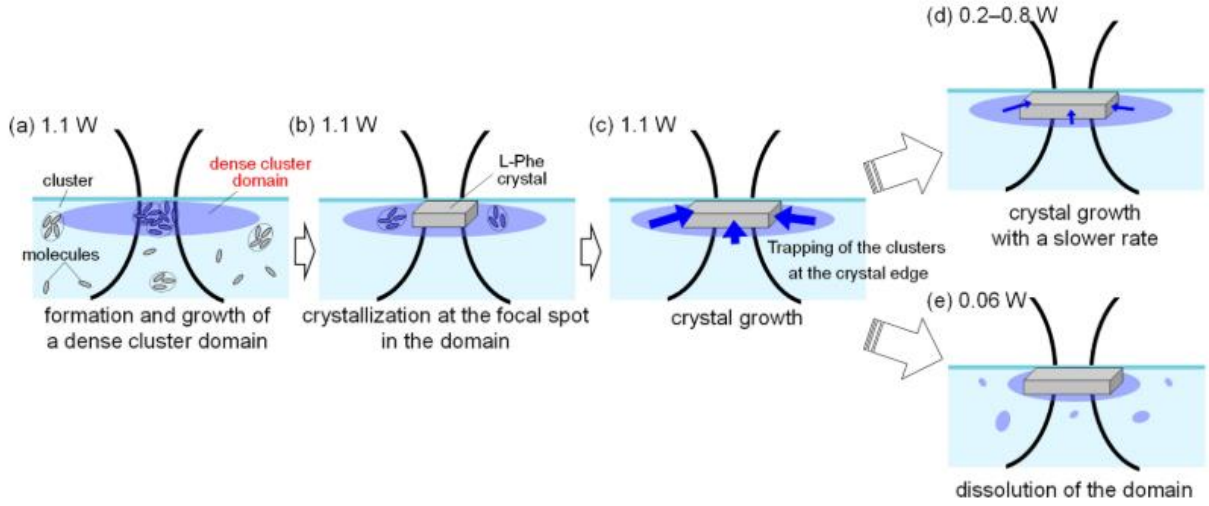

Figure 1.7 Schematic illustration of the laser trapping-induced crystallization.

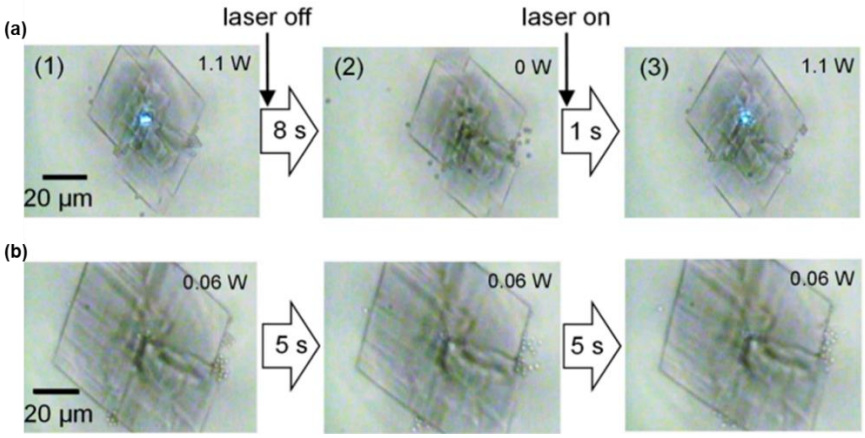

Figure 1.8 The transmission images of adding PS MPs into the solution with laser trapping induced crystal. Upper: 1.1 W. Lower: 0.06 W of the power for the trapping laser.

1.3 Femtosecond laser pulse-induced impulse

Discovery of laser has aroused a huge revolution for both scientific and technological applications, especially after realization of an intense ultra-fast pulsed lasers by Mourou and Stricktland, laureates of 2018 Nobel Prize in physics, in the 1980s

[21]. Highly intense and ultra-short laser pulses could be achieved in assistance of chirped pulse amplification technique and became a versatile tool for a wide variety of research fields. For example, with ultra-short laser pulse duration in a range of 10^{-12} – 10^{-15} seconds, instantaneous chemical reactions at the atomic level could be initiated and analyzed, which facilitates development of photochemistry and spectroscopy [22]. When transient photon density is higher than a certain threshold value, a nonlinear photomechanical phenomenon, laser ablation, is induced. Under such conditions, a part of laser focal area where illuminated at the target material can be removed from its surface, physical perturbations to its surroundings are generated, and even cavitation bubbling takes place if excess liquids like water exist [23]. During the last two decades, several kinds of cell manipulation methodologies utilizing the femtosecond laser amplifier and optical microscope have been developed. Including not only the effective multi-photon absorption, but mechanical phenomena occurring with the intense pulse irradiation [24].

The intense pulse from the femtosecond laser amplifier efficiently generates a shockwave without mass transfer of bulk water propagates at supersonic speeds and pushes on the surrounding material. The shockwave emission induces a stresswave propagation with the mass transfer and an explosive evaporation at the focal point, which is called cavitation bubble generation. The transient force resulted in these phenomena which creates precise and confined damage on a small targeted spot, acting on targets near the focal point as an impulse force [25]. The basic principle of shockwave generation including the light absorption is described based on the model of the major substance, water. The overall process is elucidated by approximating the water matrix as a semiconductor. When an intense ultra-fast laser pulse is focused at the object, a plasma formation occurs with high density free electrons at the laser focal point under the strong

electric field of the laser (**Figure 1.9**). An electron gains enough kinetic energy from the electric field of laser (photo-excitation) and escapes from confinement of local potential barrier of a molecule to be a free electron, which is called photo-ionization. This escaping electron is kept accelerating in the strong electric field of laser. As it accumulates enough kinetic energy, this speedy free electron would bring out another free electron by collision with an atom or a molecule, which is called impact ionization process. Repeatedly, these two free electrons absorb energy and make collisions again for more free electrons, which initiates an electron avalanche process to produce appreciable densities of free electrons as a plasma within a short time. Moreover, the emitted electrons as quasi-free electrons are accelerated by an electromagnetic field of the pulse. The electrons also absorb the pulse energy during the acceleration process is referred to inverse bremsstrahlung. Because electronic states of a water molecule are simply treated as valence bands and conduction bands in the approximation, photo-excitation and photoionization of the water molecules correspond to the generation of a quasi-free electron in the CB. When ionized water molecules are generated at high concentration with an intense laser excitation, the ionized molecules are explained as a plasma state with high-concentration quasi-free electrons. The plasma relaxation induces an explosive morphological change resulting in dielectric breakdown and shockwave generation.

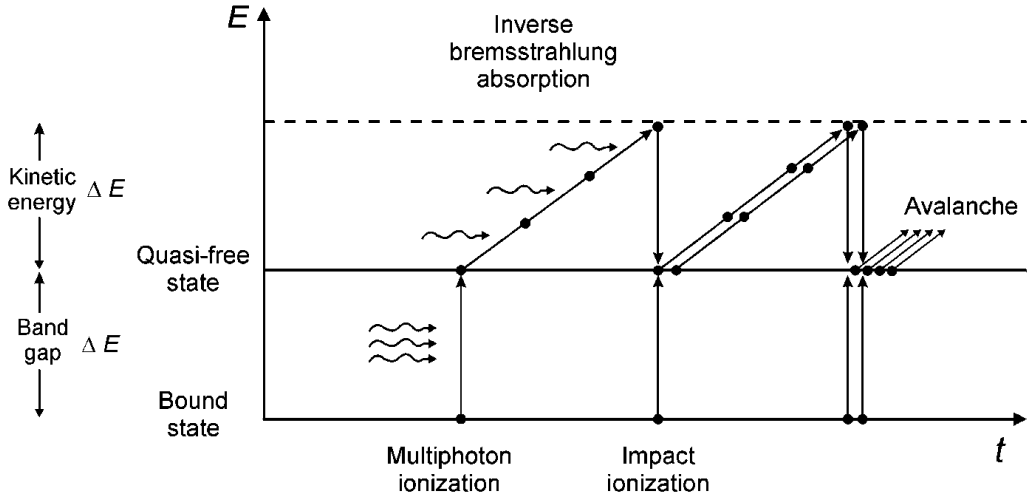

Figure 1.9 Visualization of photoionization, inverse Bremsstrahlung absorption and impact ionization leading to photoinduced breakdown and plasma forma

The heat effect and the morphology change as the function of the time after occurring the absorption was also studied in the experimental investigation of laser ablation molecular materials using single pulse [26]. As shown in **Figure 1.10**, time delay between the generation of vibrational excited energy (heat energy) and movement of bulk water, is the dominated factor. The speed of the shock wave is conceded the fast-compressional wave, sound wave. For the case of the nanosecond region, sound only travels about 10 nm within 10 ps (e.g. picosecond or femtosecond laser). This short distance in the individual molecular movement, suggesting the movement of the bulky molecular group due to intermolecular vibration is hardly induced. The nonequilibrium molecular vibration confined in the molecule results in pressure increase at the excitation area. In this process, heat energy is not converted to random kinetic energy, resulting in temperature elevation at the excitation area, but it is converted to translational kinetic energy of bulk water, which induces shockwave and stresswave emissions. Soon after shockwave is emitting, leading to the pressure decrease at the laser focal point (excited

area). The boiling point also decrease due to the decrease of the pressure, inducing the water vaporization at low temperature. Of note, this is the generation of the cavitation bubble process by shockwave emission with less temperature elevation. In contrast, nanosecond laser pulse irradiation has the nanosecond scale duration time. Such long-time excitation of the pulsed laser most likely increases the distance between inter-molecules. Instead of decrease of the pressure takes place that of the femtosecond pulse irradiation, the vibrational motion of intra and inter-molecules elevates the temperature. The sequentially generated cavitation bubble due to temperature evaluation expanding instantaneously leads to the translational molecular motion of bulk water, resulting in the emission of a shockwave and stresswaves. Noteworthy, the dynamics of nanosecond laser pulse irradiation is in reverse order to the former one explained for the femtosecond pulse irradiation. Specifically, the dynamics of nanosecond and femtosecond laser pulse irradiation are induced simultaneously, while the contribution portion depends on the pulse duration. These two distinct processes clearly exhibit the importance of pulse laser duration time.

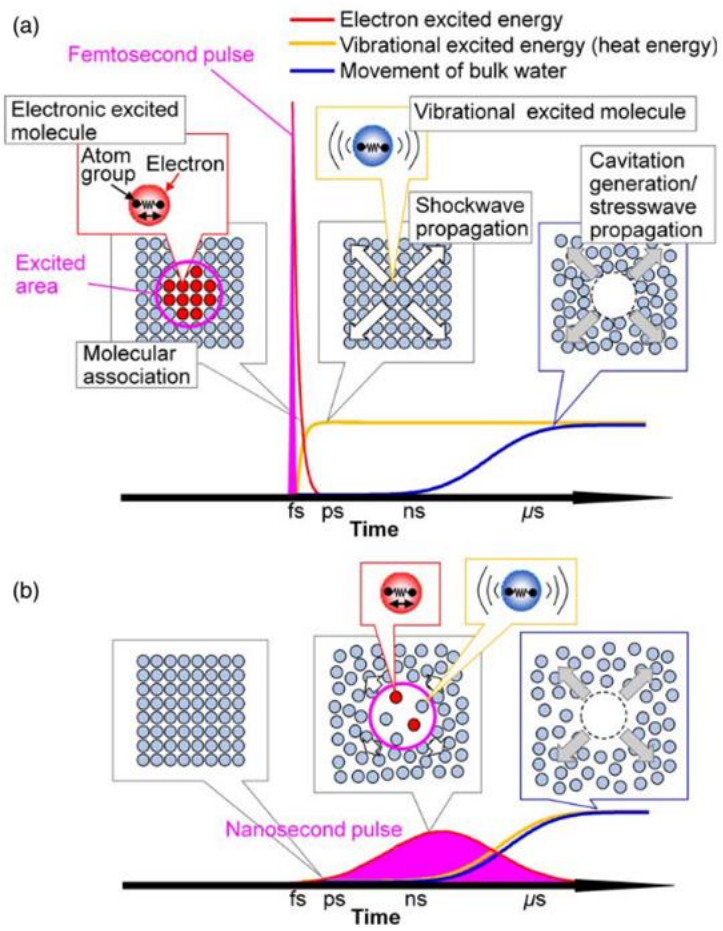

Figure 1.10 Molecular motions induced by pulse irradiation of (a) femtosecond and (b) nanosecond duration [25].

1.3.1 Mechanical property evaluation by induced impulse

Our group has been studying on this impulsive force induced by a femtosecond pulsed laser (fs-laser). When a single intense fs-laser pulse is focused at the solution or objects, it has been proved that ablation is induced following with the cavitation bubble and a shockwave generation. The shockwave exerts on the objects as the impulsive force, allowing several applications such as detach individual adherent cells without causing considerable cell damage, control of the position change for the surrounding objects under the microscale and the evaluation of the mechanical property (As shown in **Figure 1.11**). Furthermore, this fs-laser induced impulsive force was uncovered with a magnitude in a

micro-Newton scale by means of atomic force microscopy [27]. The estimation of the fs-laser induced impulsive force can benefit in the micro-biology field and the development of materials such as quantification of the adhesion strengths between cells or between cells and scaffold and detection of the surface mechanical property of the complex micro-objects like embryos.

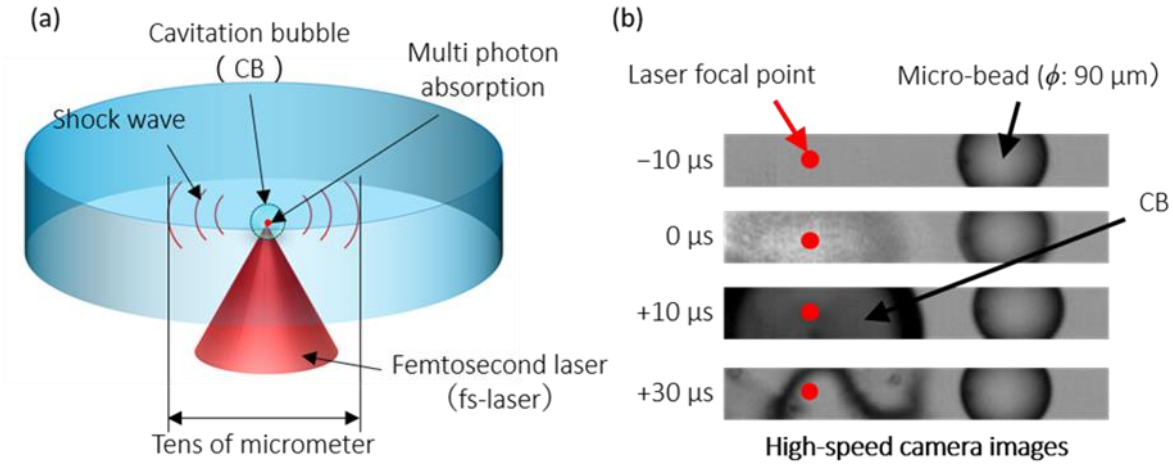

Figure 1.11 (a) Illustrative scheme of an impulsive force generated by a fs-laser (b) Demonstration of an impulsive force to change the position of surrounding objects through a cavitation bubble and a shockwave (from our group)

As a representative mechanical parameter, Young's modulus, is essential for investigation for materials stiffness. Generally, the AFM indentation test has been widely applied for evaluating it in μm-scale elastic materials This tensile test is commonly used to measure Young's modulus for entire sample objects. The indentation test is also permitting Young's modulus mapping, even at the single cellular level utilizing with an AFM cantilever. In this test, the AFM cantilever is contacted on the object to detect the indentation as a function of the force applied by the cantilever [28]. From the obtained force-indentation curve from AFM force spectroscopy, Young's modulus is estimated based on Hertz con-tact theory as a measure of the apparent stiffness. However, this AFM

indentation test usually delivers the information contains of entire object (i.e. the average Young's modulus of the objects.) In addition, this simple indentation test allows mechanical property of isotropic material to be evaluated though, this method is insufficient for anisotropic material like protein crystal. In the context, there is a demand for a more flexible evaluation method for the elasticity of the specific part like the surface.

Our group has developed an original method, pulsed-laser-activated impulse response encoder (PLAIRE) by taking the advantage of the detection of elastic waves. Due to the feature of containing the structural information of the objects depending on where the excited vibration propagates, this main advantage of this impulse excitation technique has been incorporated with our developed technique, PLAIRE. In this method, an infrared femtosecond laser pulse is focused on or nearby a micro-scale object into the aqueous solution under a microscope. The laser irradiation induces an explosion at the laser focal point with highly efficient multiphoton absorption. The area of localized explosion is around 1 μm, generating a stress wave that propagates to the object. The wave vibration is detected by an AFM cantilever attached to the object. The cantilever is capable to detect vibrations in the surface specifically resulting from the excitation of the elastic wave propagating along the surface. Analyzing the vibration systematically to calculate Young's modulus enables the specific evaluation of mechanical properties for the objects [29]. As shown in **Figure 1.12** [30].

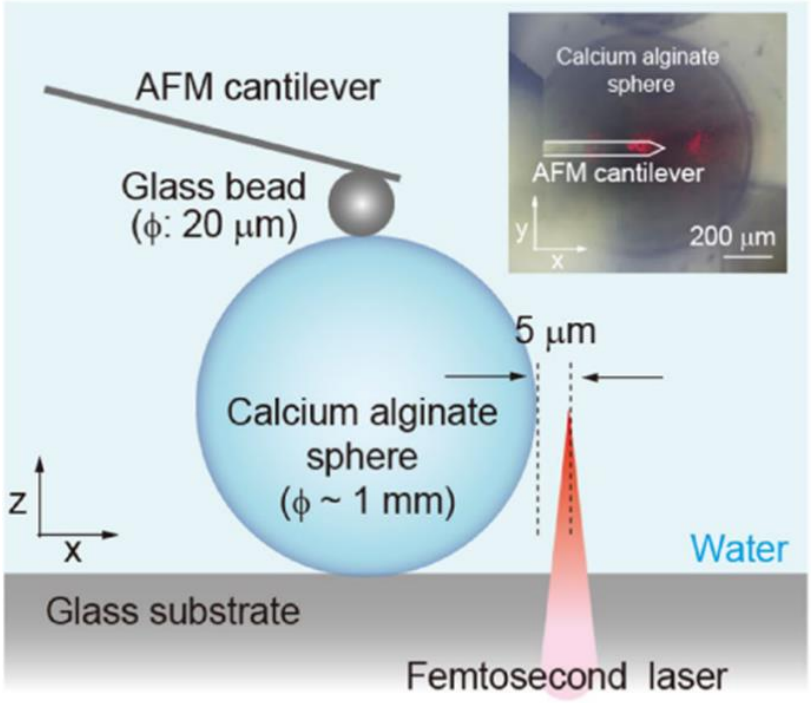

Figure 1.12 Relative configuration of the laser focal point, the AFM cantilever and the CaAlg gel-sphere. *(Inset)* An image of AFM cantilever placed on a CaAlg gel-sphere taken by the upright low-magnification microscope

1.4 Structure of this thesis

The main objective of my study is to applied laser micro-manipulation techniques to achieve micro-scale control and evaluation of the protein assembly, which are optical trapping for its fabrication and PLAIRE for its evaluation. As described in the **section 1.1**, protein assembly can be engineered in several fields, for example, function as the protection agent to applied for food industry. Through this study, we aim to fabricate the protein micro-assembly in a non-destruction and non-intrusive manner and evaluate the mechanical stiffness of protein assembly with and without discussing its surface properties.

The first goal, in the optical trapping experiment, formation of a single submillimeter-sized lysozyme assembly was demonstrated and dynamics for its formation was clarified by adding polystyrene microparticles and dye-labeled lysozyme. The second goal, in the experiment by PLAIRE, Young's modulus of a single micro-crystal of lysozyme was systematically evaluated. Herein, below showed how I approached my goal step by step as described in the chapters below:

Chapter 1-Introduction: To introduce the required background knowledge for establishing and achieving the goal on the basis of understanding its requirements and significance. The principle and specialty for optical trapping and pulsed laser induced-impulse is included in this chapter.

Chapter 2-Experimental setup: To interpret how my optical micro-manipulation system was constructed and working under the cooperation of various components, including the sample preparation for all kinds of experiments. Of note, the laser sources of optical trapping and PLAIRE technique are different. A continuous-wave laser is chosen for optical trapping-fabricated protein assembly. In the contrast with, femtosecond laser is

chosen for PLAIRE technique to evaluate the protein crystal stiffness.

Chapter 3-Fabrication of protein assembly: In this chapter, optical trapping-fabricated lysozyme assembly and its morphology determination by incorporating microparticles is described. The discussion of several conditions changed of protein assembly, such as concentration, over the trapping laser irradiation by means of various microscopy technique.

Chapter 4-Mechanism of protein assembly: In this chapter, dynamics and mechanism of the optical trapping-fabricated lysozyme assembly is interpreted using dye-labeled lysozyme and synchronized imaging. Two-stage optical trapping behavior is proposed to elucidate protein assembly under optical force based on the systematic investigation of incident laser power and the initial concentration of the protein.

Chapter 5-Protein crystal evaluation: In this chapter, mechanical property of protein crystal is evaluated utilizing our developed technique, PLAIRE, the application of fs-laser induced-impulse in comparison of the conventional method, AFM indentation method, based on Hertz contact theory. PLAIRE technique is developed for the detecting the surface stiffness of the targets specifically.

Chapter 6-Conclusion and perspective: In this chapter, the results and the findings are summarized and clearly pointed out the novelty of this study. Perspective and potential experiment to extend this research is proposed as well.

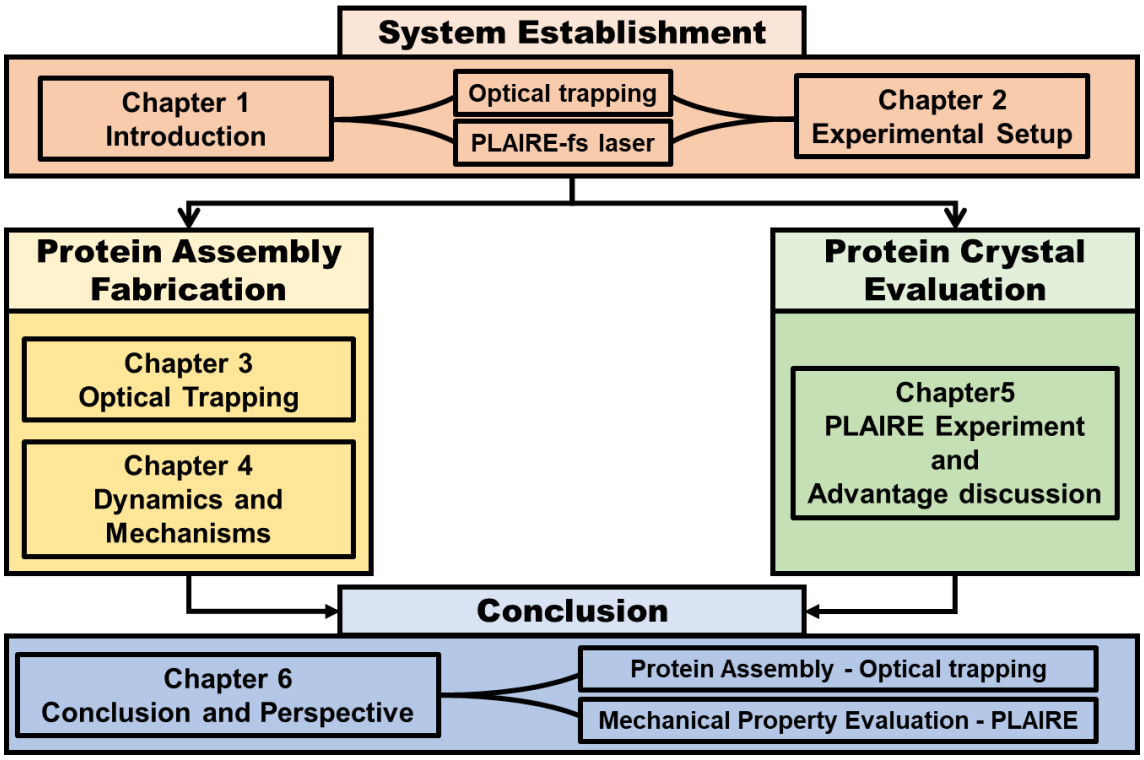

Figure 1.13 Structure and the flow chart of this thesis.

Chapter 2 Experimental

2.1 Sample preparation

2.1.1 Hen egg white lysozyme solution

For the protein assembly fabrication experiment, hen egg white lysozyme is chosen as the target due to its well-known and studied feature. Lysozyme, also referred to muramidase or N-acetylmuramic hydrolase, is a small, monomeric protein stabilized by four disulfide linkages among the eight cysteine residues of its polypeptide chain, **Figure 2.1** [31]. Regarding the application, lysozyme has been allowed for use in the food industry, killing bacteria and eliminating fungi.

Hen egg white lysozyme (FUJIFILM Wako Pure Chemical Corporation, Model No. 127-06724) was used as received in our protein assembly fabrication experiment. We adjusted the concentration of lysozyme to 300 and 375 mg/ mL corresponding to 20 and 26 mM, respectively. We prepared one lysozyme stock solution by dissolving lysozyme powder into D_2O solvent (Sigma-Aldrich, 99.9 atom %) rather than H_2O solvent. Because 1064 nm laser which was used in optical experiment, is absorbed by the overtone vibrational modes of H_2O and the resultant temperature elevation is 23 K/W [32]. Thus, we used D_2O as a solvent to reduce the laser-induced temperature elevation almost 1 order of magnitude, so that we could consider that temperature elevation effect is not appreciable. The prepared lysozyme solution was filtered with a syringe filter (pore size 0.22 μm, SLGVX13NL, Millipore) to remove large aggregates or dust. As the solubility of lysozyme in H_2O is reported to be 366 ± 10 mg/mL [33], so that our latter solution may be a little supersaturated solution. Considering the molecular weight of lysozyme (14300 Da) and D_2O (20 Da), the molecular number ratio of D_2O to lysozyme is estimated to be

about 2000:1. As the viscosity of lysozyme aqueous solution of 342 mg/mL is reported to be 20 cP,31 the present D_2O solution of 375 mg/mL must be more viscous. The pD value is 5.1, replaced pH by the correction of adding 0.4 to the measured value of a pH meter (Beckman Coulter, pHi510) [34]. The absorption spectrum of the lysozyme solution was measured in the range of 350 nm to 1000 nm. Prepare the measured sample by filling the concentration-series of lysozyme to the quartz cuvette with the optical path of 1 mm (Starna Scientific). Measurement is with a UV-VIS-NIR spectrometer (Jasco, V-670). The obtained absorbance (A) value was plotted with the length of the optical path (d) and fitted with the relation from Beer-Lambert law:

$$A = \varepsilon bc$$

Where ε is the molar attenuation coefficient or absorptivity of the attenuating species; b is the optical path length in cm; and c is the concentration of the attenuating species. The absorbance of lysozyme as the function of the incident light wavelength is plotted as the shown in **Figure 2.2**.

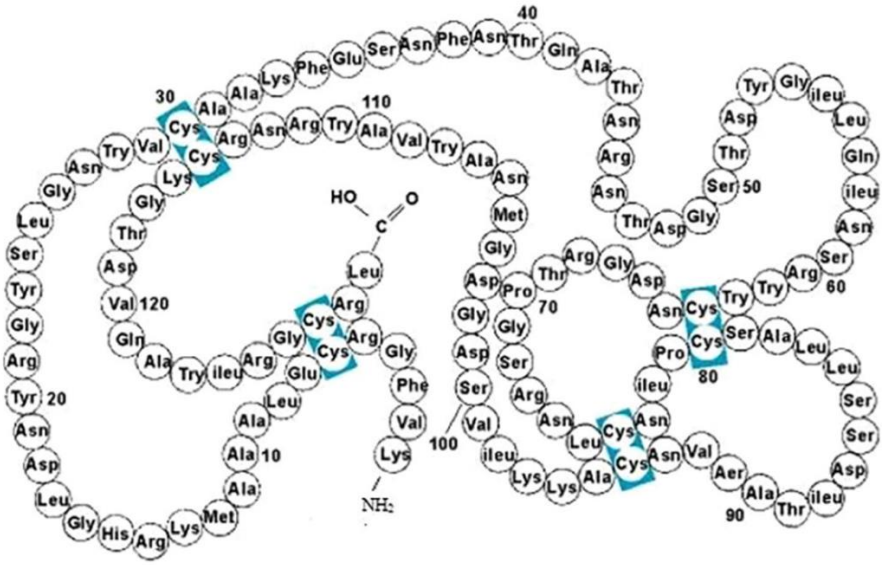

Figure 2.1 Structure of lysozyme in the single chain mode, containing of 129 amino acid.

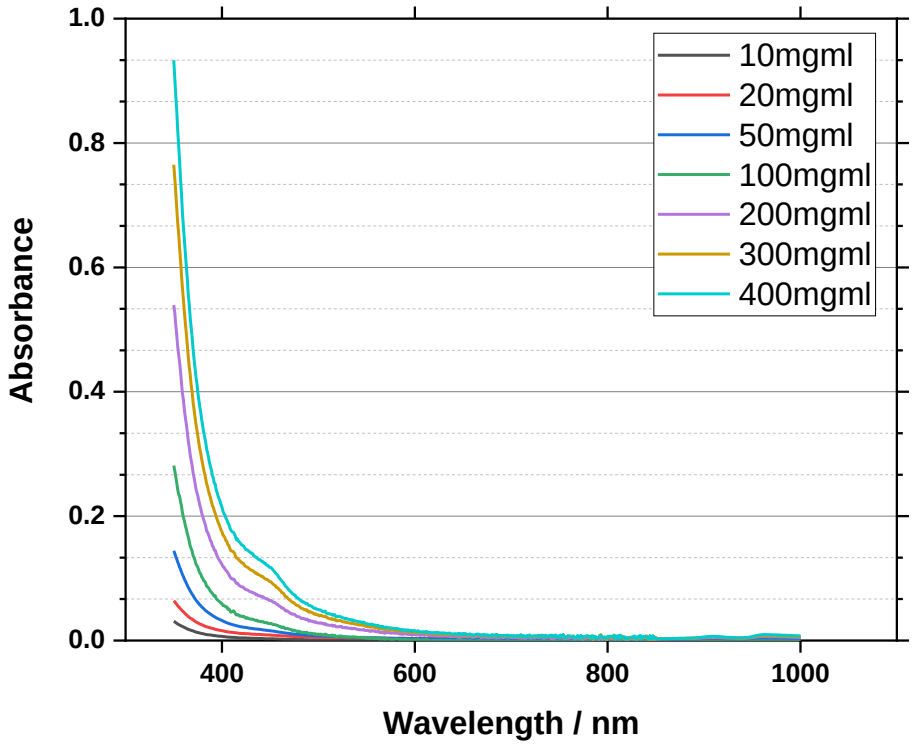

Figure 2.2 The absorption spectra of lysozyme solution with concentration dependence.

For the chamber where the sample solution is dropped into, the cover class (Matsunami, NEO micro cover glass, 24 × 32 mm, thickness 0.12~0.17 mm) with was sandwich-glued with a glass ring using silicone caulk (Shin-Etsu Silicone, KE 3490) (as shown in **Figure 2.3**). Before the chamber constructed, glass slides are immersed in the water with 10% v/v detergent solution (Hellma Analytics, Hellmanex III) and being sonicated for 15 minutes in order to remove contamination and to increase the hydrophilicity of the glass surface. The sample solution of 15 μL was intentionally dropped in the center of the chamber without contacting the wall of the chamber to avoid the uni-direction flow.

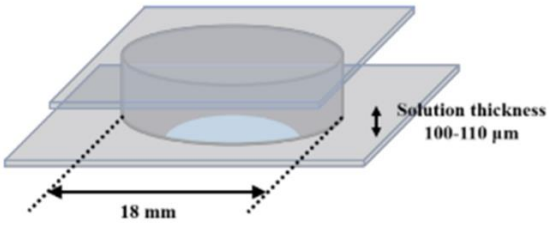

Figure 2.3 A schematic illustration of the sample chamber with the sample droplet. Diameter of the chamber is 18 mm. The height of the droplet is 100 – 110 µm

2.1.2 Dye-labeled Lysozyme

As the absorption spectrum of regular lysozyme only involve in the UV-region. Due to tryptophan, tyrosine, and phenylalanine, contributing to the intrinsic fluorescence lysozyme whose central emission light wavelength is around 400 nm [35] (**Figure 2.4**). Since the shortage of the corresponding light source to excite the lysozyme intrinsic fluorescence, the commercial dye-labeled lysozyme is an alternative to obtain the fluorescence image with our current experimental setup. The quantum yield of rhodamine B (RhB) is 0.31 in water where quantum yield refers to the ratio of the number of photons emitted divided by the number of photons absorbed [36]. It is obvious that RhB can be excited with relatively low intensity excitation laser with the appropriate wavelength (as shown in **Figure 2.5**) [37]. Hence the RhB-lysozyme is a good candidate for our experiment, which is commercially available (NanoCS, Model No. LS1-RB-2). We treat the RhB lysozyme as received without any purification or modification and add it in the regular lysozyme with the ratio of 1:10000. The excitation and emission spectra of the condition of our sample use were carried out with the spectrometer (HORIBA FluoroMax-4), as shown in **Figure 2.6**. Based on the obtained spectrum, a 532 nm laser is capable for fluorescence imaging. The calibration curve is was checked for quantify the concentration determination (**Figure 2.7**). In the graph, total lysozyme concertation is

fixed; however, the relative amount of the RhB lysozyme is proportional changed as the varied factor (x-axis). As the result, we consider the linearity relation between lysozyme concentration and fluorescence intensity to be reliable.

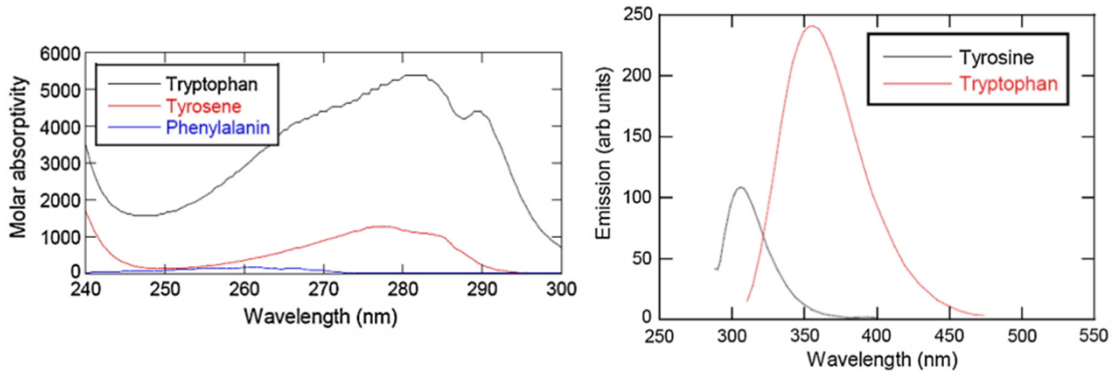

Figure 2.4 Left: The absorption spectra of the aromatic amino acid in lysozyme. Right: The emission spectrum for tryptophan and tyrosine excited at 266 nm

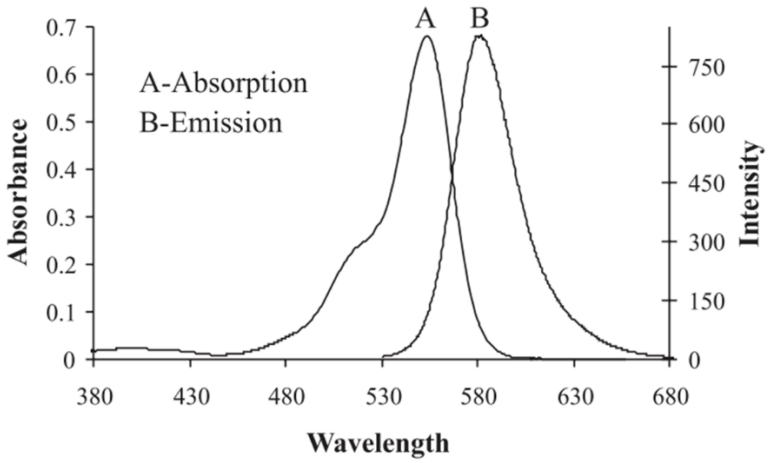

Figure 2.5 Absorption (A) and Emission (B) spectrum of rhodamine B.

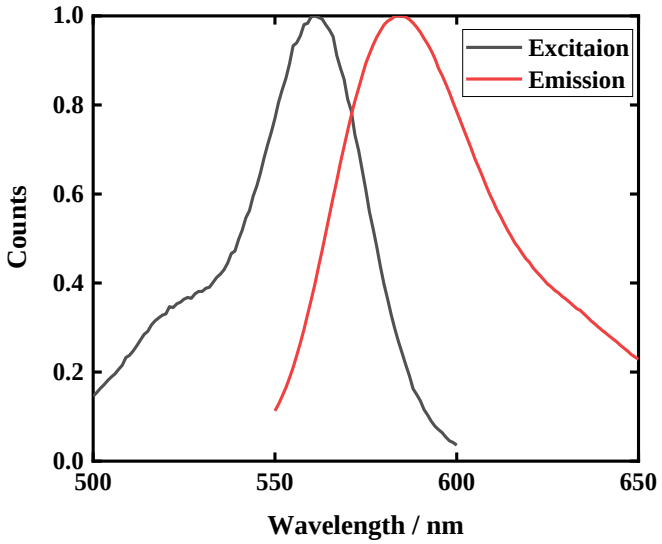

Figure 2.6 Excitation (black) and Emission (red) spectrum of rhodamine B labeled lysozyme. The counts are normalized to each maximum value.

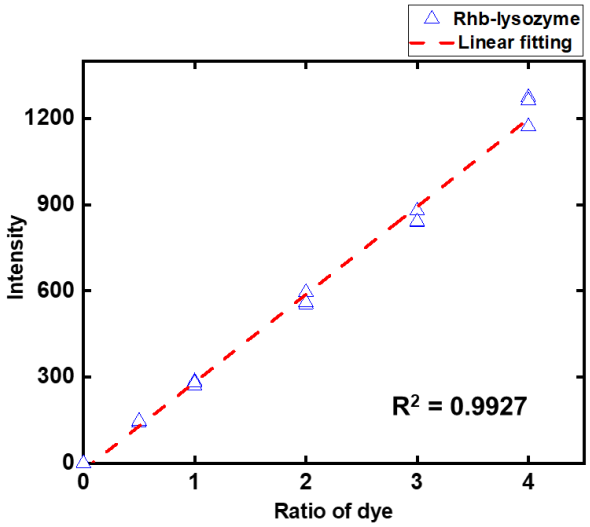

Figure 2.7 The calibration curve to confirm the reliability of the linearity between the rhodamine B concentration and its fluorescence intensity.

2.1.3 Crystallization

For the protein assembly evaluation, lysozyme crystal which is widely used for investigating basic properties is chosen as a model for evaluating the mechanical property.

A lysozyme powder (FUJIFILM Wako Pure Chemical Corporation, Model No. 127-06724) was dissolved into H_2O acetate buffer solution with 100 mM. The initial sample solution was adjusted (lysozyme 30 mg/mL; NaCl 3.0% (wt.); pH = 5.0) by mixing equal volumes of the lysozyme stock solution and the NaCl 6.0% with acetate buffer solution. The solution was filtered with a sterile syringe filter (Hawach Scientific, pore size: 0.22 μm, SLPES2522S) to remove the large aggregates or dust. Micro-lysozyme crystals were precipitated by dropping 1 mL of the solution into the glass bottom dish (ibidi GmbH35 mm) without covering and placing in an incubator (Tokyo Rikakikai, LTE-510) in stationary at 15 degree Celsius until the spontaneous evaporation was completed (**Figure 2.8**). It is noteworthy, the lysozyme crystal is stuck to the glass bottom dish after water is completely evaporated. It most likely the cause of the charge balance, since at given condition lysozyme molecules carry the positive charge; on the other hand, glass bottom dish may carry the opposite. Through the microscope, the length of the crystals reaches to about 1 mm. **Figure 2.9** shows the observation of submillimeter-sized lysozyme crystal under our experimental microscope condition and the corresponded position between laser focal point and AFM cantilever.

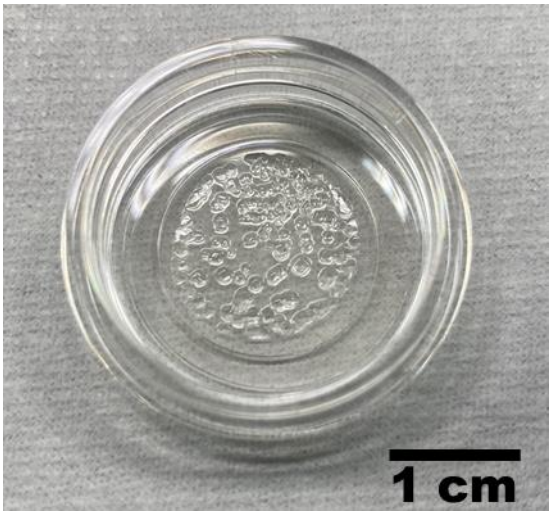

Figure 2.8 The photograph of the spontaneous-evaporated lysozyme crystal.

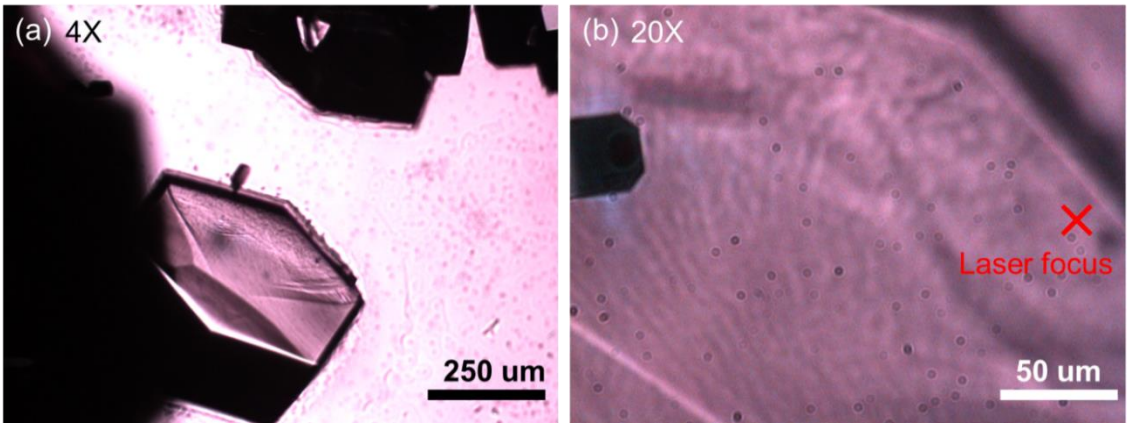

Figure 2.9 Transmission images of lysozyme crystal. (a) Lysozyme crystal observed with objective lens 4X. (b) The AFM cantilever (at the left of the image) placed on a lysozyme crystal with objective lens 20X. The red cross indicates the laser focal point.

2.1.4 Colloidal particles suspension solution

A commercially available colloidal suspension of 0.75 1, 3, 4.5, 6, and 10 μm-sized PS MPs (Polyscience Inc., Polyscience Inc., #07759-15, #08226-15, #09850-5, #17140-5, #17141-5, and #18133-2, respectively) were dispersed well in H_2O initially, as their surface is carboxylated, having −COOH substituents. Their concentration was adjusted to be 2.26×10^{-4} particles/μm^3. Firstly, the initial H_2O of PS MPs suspension solution is withdrew after the centrifugation. The prepared lysozyme solution with D_2O as the solvent then next filled in, resulting the mixed solution composed of PS MPs and lysozyme in D_2O solution. The effective volume of the laser focus is in the order of μm^3, so that, under this concentration, no MP is found inside the focus. Thus, all the MPs were gathered by optical force during the laser irradiation. The density of PS is 1.05 g/mL and higher and lower than H_2O (1.00 g/mL) and D_2O (1.11 g/mL), respectively. Thus, the PS MPs receive buoyance in D_2O and they are pushed up to the solution surface. As the density difference between PS and D_2O is not large, initially PS MPs are well dispersed in solution after the solution preparation. We usually waited for 3−5 min after preparing

samples and started experiments, preventing the undesired convection flow.

2.2 Optical setup

The optical setup is categorized into 3 parts according to their purposes: (1) optical trapping coupled with fluorescence imaging and Raman microspectroscopy for protein assembly fabrication and examine its morphology. This work was done in National Yang Ming Chiao Tung University, Taiwan, (2) Simultaneously transmission imaging and fluorescence imaging for elucidating the dynamics and the mechanism of lysozyme assembly. This experiment was initiated in Katholieke Universiteit Leuven, Belgium. (3) PLAIRE: Pulsed-laser-activated impulse response for the evaluation of the crystal mechanical properties. The work was completed in Nara Institute of Science and Technology, Japan. The continuous-wave laser was used in the optical trapping experiment of (1) and (2) for gathering the protein molecules. The fs-laser pulse was applied for the PLAIRE experiment of (3) for laser-ablation.

2.2.1 Optical trapping coupled with fluorescence and Raman measurement

The experimental setup is given in **Figure 2.10**, where a 1064 nm trapping laser (Spectra Physics, J20I-BL-106C) was combined with an inverted microscope (Olympus, IX71). The trapping laser was focused on the solution surface through an air-immersion objective lens with the numerical aperture of 0.90 and the magnification of 60 (Olympus, UPLFLN60X, Semi-Apochromat Objectives). The laser power after the objective was set to 1 W with a combination of a half-wave plate and a polarizing beam splitter. This corresponds to 70 MW/cm^2 at the sample, which was best for preparing respective assemblies of PS MPs and lysozyme and for measuring their formation dynamics. A 532 nm laser was introduced additionally as an excitation beam for fluorescence imaging and

Raman scattering spectroscopy, whose power density was adjusted to be 140 W/cm^2 (widefield) and 5 MW/cm^2 (at the focal spot), respectively. In addition, a 532 nm laser can also be an indicator, monitoring the solution surface before and during the trapping irradiation.

The transmission and fluorescence images were recorded with a CCD camera (Watec France, WAT-231S2), while Raman spectroscopy was obtained with a polychromator (Andor Technology, SR-303i-A) equipped with a CCD camera (Andor Technology, DU920P-BV). The illumination source of the transmission imaging is from halogen lamp in a trans-illumination fashion coupled with a condenser lens with numerical aperture of 0.30. The objective lens stage is motorized, and its height can be computer-controlled.

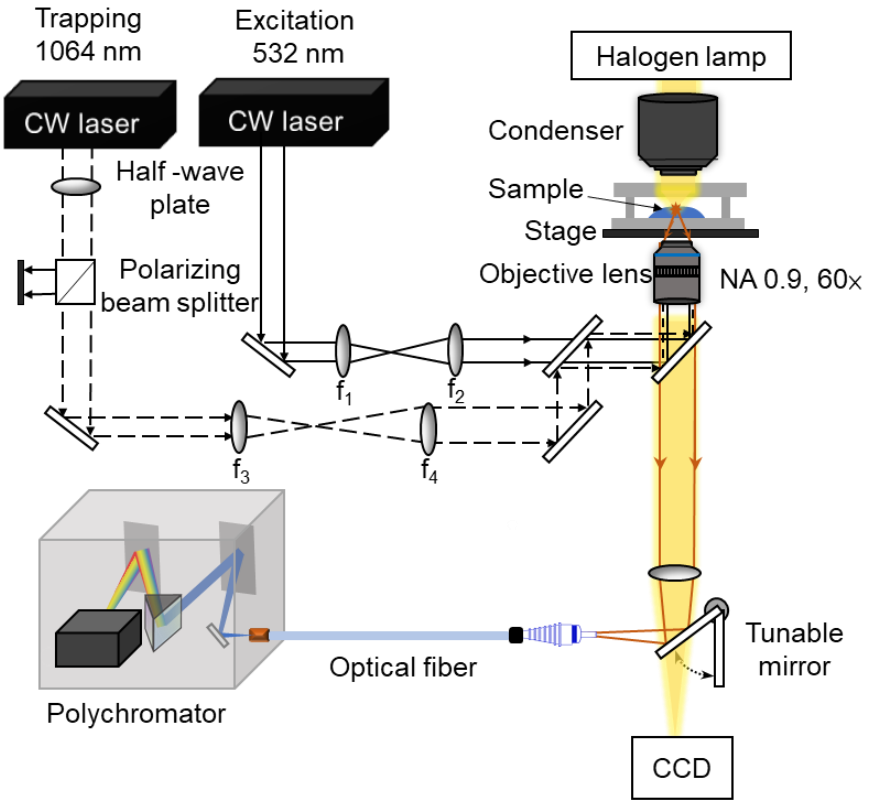

Figure 2.10 Experimental setup for optical trapping, Raman spectroscopy measurement, and fluorescence imaging. Objective lens (NA 0.9, 60×) and condenser lens (NA 0.3) are used for trapping/imaging/Raman and illumination in transmission imaging, respectively. The objective

lens stage is motorized, and its height can be computer-controlled.

2.2.2 Simultaneous transmission imaging and fluorescence imaging

The optical scheme of the used widefield multiplane microscope is shown in **Figure 2.11**. A 488 nm laser line was used as widefield excitation laser by focusing it at the back focal plane of an air-immersion objective lens (NA 0.90, 60x, Olympus UPlanFLN 60X). The laser widefield irradiance is controlled by neutral density filters. Simultaneously, a 1064 nm continuous wave laser is tightly focused at the upper solution/air surface by the same objective lens. The trapping laser power is controlled by a combination of a half-wave plate and a polarized beam splitter. A halogen lamp illuminates the sample through a Köhler condenser lens after selecting the red and infrared light using a 655 nm long pass filter. A 640 nm indicator laser was introduced to localize the surface position at the corner of the images. The transmitted and fluorescence emitted light by Rhodamine B-Lysozyme conjugate is collected by the same objective lens and filtered by a 1010 nm short-pass optical filter to remove the 1064 nm laser backscattered light. The transmitted/emitted light went through a set of lenses in telecentric 4f configuration [Objective - Lens1 – field stop - Lens2 - Tube lens – Camera(s)]. The field stop was used to control the size of the image. Between the tube lens and the cameras, we placed a proprietary prism, which splits the entering photon flux into eight different beams with slightly different optical path lengths. The different imaging planes were recorded by 2 CMOS cameras (4 imaging planes for each camera, Orca Flash 4.0, Hamamatsu Photonics Inc.). To gain the spectral resolution, we placed a 570 ± 50 nm (fluorescence of Rhodamine B-Lysozyme conjugate) or a 675 ± 30 nm (transmitted red and NIR light) band-pass optical filter in front of each camera, respectively. The upper right inset of **Figure 2.11**, showing the wavelength regions of two CMOS cameras which simultaneously capture. To ensure a correct

synchronization of the two CMOS cameras, we triggered the acquisition via a National Instruments board (NI, USB-6343) coupled to a home-built software written in Labview. As in this case, we do not require a 3D transmission/fluorescence image, we will only analyze a single image per camera (i.e., one CMOS camera will provide the fluorescence image, while the other CMOS camera will provide the transmission image).

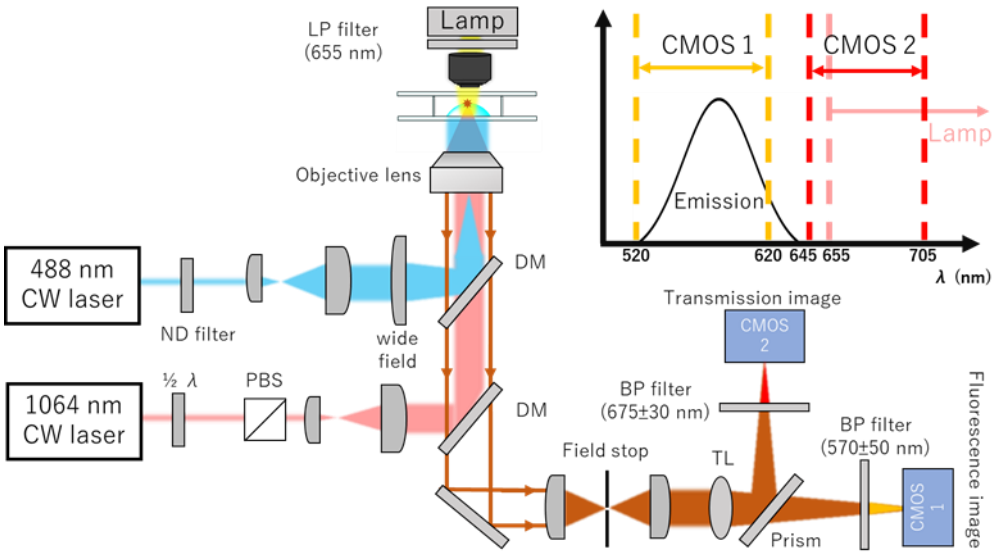

Figure 2.11 An experimental setup for optical trapping and transmission and fluorescence imaging. Objective (NA 0.9, 60×) and condenser (NA 0.3) lenses are used for trapping and transmission imaging, respectively. The upper right inset shows the wavelength regions of two CMOS cameras which simultaneously capture transmission and fluorescence images. The different imaging planes were recorded by 2 CMOS cameras (Orca Flash 4.0, Hamamatsu Photonics Inc.).

2.2.3 PLAIRE: Pulsed-laser-activated impulse response encoder

The experimental setup is given in in **Figure 2.12**. A single laser pulse from a regeneratively amplified Ti:sapphire femtosecond laser (Spectra-Physics Solstice-Ace, 800 nm, 100 fs, 20 Hz) was introduced to an inverted microscope (Olympus IX-71) and

focused at the upper surface of a lysozyme crystal (110-plane) directly through a 20× objective lens (Olympus, UMPlanFl, 1-UN525, N.A. 0.46). The single pulse was extracted using a mechanical shutter with a ~30 ms gate time. The pulse energy was tuned at 3 μJ/pulse by polarizers and neutral density filters. As shown in Figure 2.12, the vibration excited on the lysozyme crystal was detected by an AFM cantilever (Nanowizard 4, JPK Instrument; Cantilever: qp-SCONT-10, Spring constant: 0.01 N/m) contacted on the crystal surface at a certain distance to the laser focal point. The temporal profile of the vibrational amplitude was recorded as cantilever oscillations. The temporal movement of the cantilever with the crystal vibration waveform due to the voltage difference between the upper and bottom sides of a quadrant photodiode inside the AFM was recorded and monitored by an oscilloscope (Tektronix DPO 4104). The vibration signal was converted to the cantilever displacement using a linear coefficient of 1.7 mV/nm. The sample-stage is motorized and its translational and axial motion can be computer controlled. (Inset) A transmission image of the AFM cantilever placed on a lysozyme crystal. Scale bar is 50 μm.

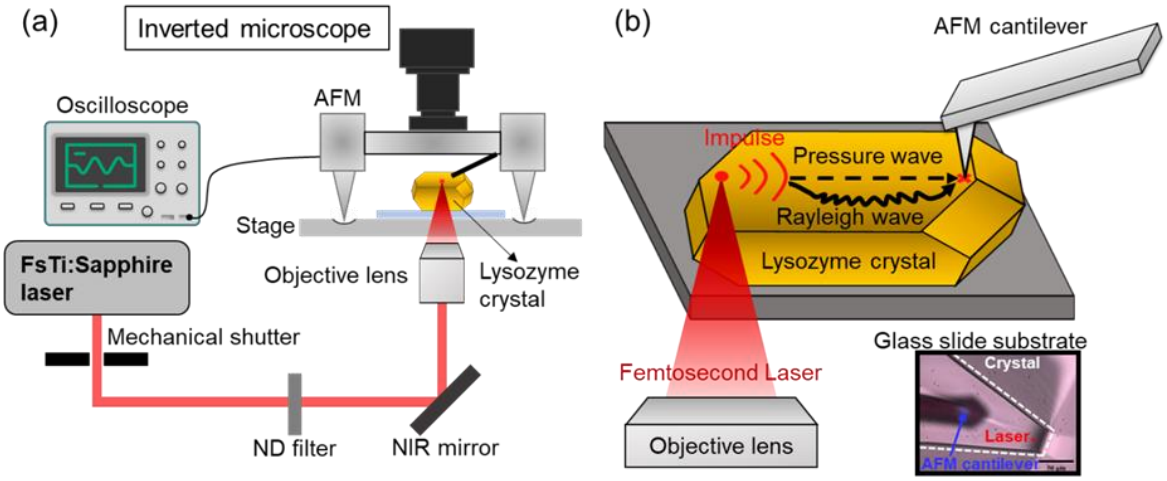

Figure 2.12 (a) Schematic illustration of the experimental setup. An objective lens (NA 0.46, 20X) is used for the transmission imaging and focusing fs laser. The stage is motorized and its

translational and axial motion can be computer controlled. (b) Schematic illustration representing the relative configuration of the laser focal point, a lysozyme crystal, the AFM cantilever and the propagations of induced waves. (Inset) A transmission image of the AFM cantilever placed on a lysozyme crystal. Scale bar is 50 μm.

Chapter 3 Optical trapping for fabricating a single lysozyme assembly

3.1 Assembly morphology under microscope

Before the laser trapping was started, lysozyme formed a layer with a thickness of a few μm at the surface, and upon the trapping laser irradiation, more lysozyme protein was collected at and around the focal point in the D_2O solution. The highly concentrated region expanded very widely and even deeply, namely, three-dimensionally, the method to determine three-dimensional structure is explained in section 3.4.3. This lysozyme assembly formation was first examined by transmission imaging. As lysozyme has no electronic absorption band in the visible wavelength region, transmission imaging is interpreted in terms of refractive index change due to lysozyme distribution. The refractive index may arise from whether the concentration difference, surface deformation or phase separation. Because optical trapping is introduced into, we assumed the locally highly concentrated domain is formed induce the observable edge. The results on its high concentration solution of 26 mM are summarized in **Figure 3.1**. After switching on the laser trapping, the focal point became black, and the dark area expanded quickly, which was accompanied by a white ring at the edge. Its diameter reached about 70 μm in 120 s. Inside the area the darkness distribution was inhomogeneous, and the central black domain moved to the left. It is explainable to assume that lysozyme is rapidly gathered initially at the focus, and then its assembly grew to the outside. The collected lysozyme has a larger and inhomogeneous distribution of refractive index, although the initial concentration was over the saturation degree. At the border between the collected area and initial solution, the refractive index change was large, giving a white ring. After

switching off the laser, the white ring shrank in a few seconds. Based on the transmission image, the phenomenon seems reversible. The ring size was measured after switching the trapping laser on and off, and the ring enlargement and shrinking are summarized in **Figure 3.1**.

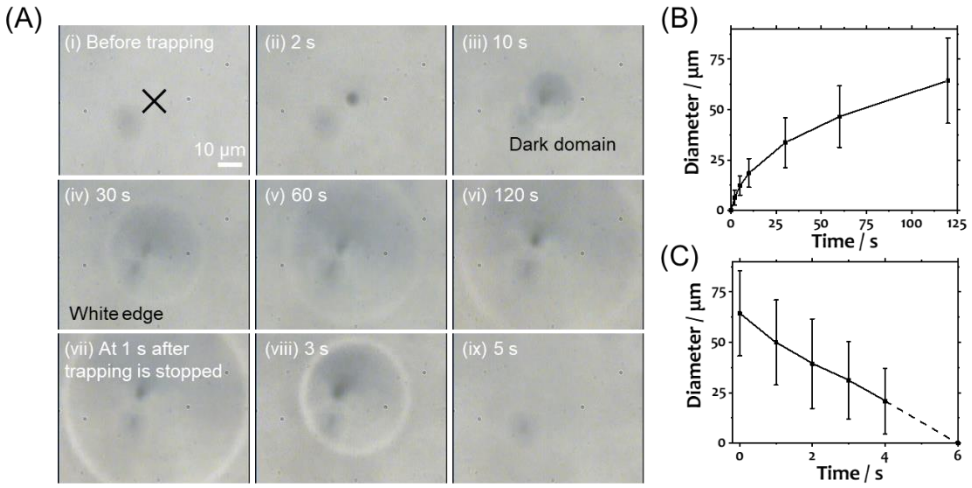

Figure 3.1 (A) Transmission images of the optical trapping-induced formation of the lysozyme assembly at the D2O solution surface of 26 mM lysozyme, showing a white ring inside which optical transmittance is inhomogeneous: (i) Before irradiation; (ii)−(vi) after switching on the 1064 nm trapping laser; (vii)−(ix) after switching off the 1064 nm laser. The scale bar is inserted in (i). An approximately 10 μm sized dark area located a little left lower was common for (A) (i) and (iv), which is ascribed to a dust in our optical system, as they were observed before switching on and at 5 s after off. (B) The diameter of the white ring increased after switching on the laser. (C) The diameter of the white ring decreased after switching off the laser

3.2 Fluorescence imaging

One clear indication of lysozyme assembly formation was given by fluorescence imaging. We added a small amount of rhodamine-B-labeled lysozyme with a ratio to lysozyme of 1:10000 and carried out the same trapping experiments. It was assumed that the trapping behavior of lysozyme was not affected by this addition. The results are

summarized in **Figure 3.2**, where a 532 nm laser is used as a widefield excitation laser. Its excitation area covers the field of view, although the excitation intensity distribution is not perfectly homogeneous, being more intense in the center over the trapping laser irradiation duration time course. The homogeneity has been corrected considering the normalizing of the images with the fluorescence image obtained before switching on the trapping laser. As shown in **Figure 3.2 (iii)−(vi)**, the diameter of the fluorescence domain expanded to a few tens μm after 60 s of irradiation. Upon switching off the trapping laser, the fluorescence domain soon disappeared and was not identified anymore at 40 s after switching off the trapping laser. The assembly expansion and shrinking in fluorescence images are similar to those in transmission images. We carefully analyze the fluorescence intensity increment utilizing the trapping time-evolved images. To begin with, we consider the image without switching on trapping laser and excitation laser as the background **Figure 3.2 (i)**, by which the following-captured fluorescence images with trapping laser irradiation are subtracted. In order to compart the fluorescence intensity before and after trapping laser irradiation, the fluorescence image which is with only excitation laser irradiation is regarded as the standard. The fluorescence image with excitation laser and trapping laser is divided by the fluorescence image which is without trapping laser, as shown in **Figure 3.2 (ii)-(ix)**. The fluorescence intensity is increased about three times afire 60 s irradiation and its distribution is indicated in the **Figure 3.3** which analyzed form the region of white dashed line cursor **Figure 3.2 (vi)**.

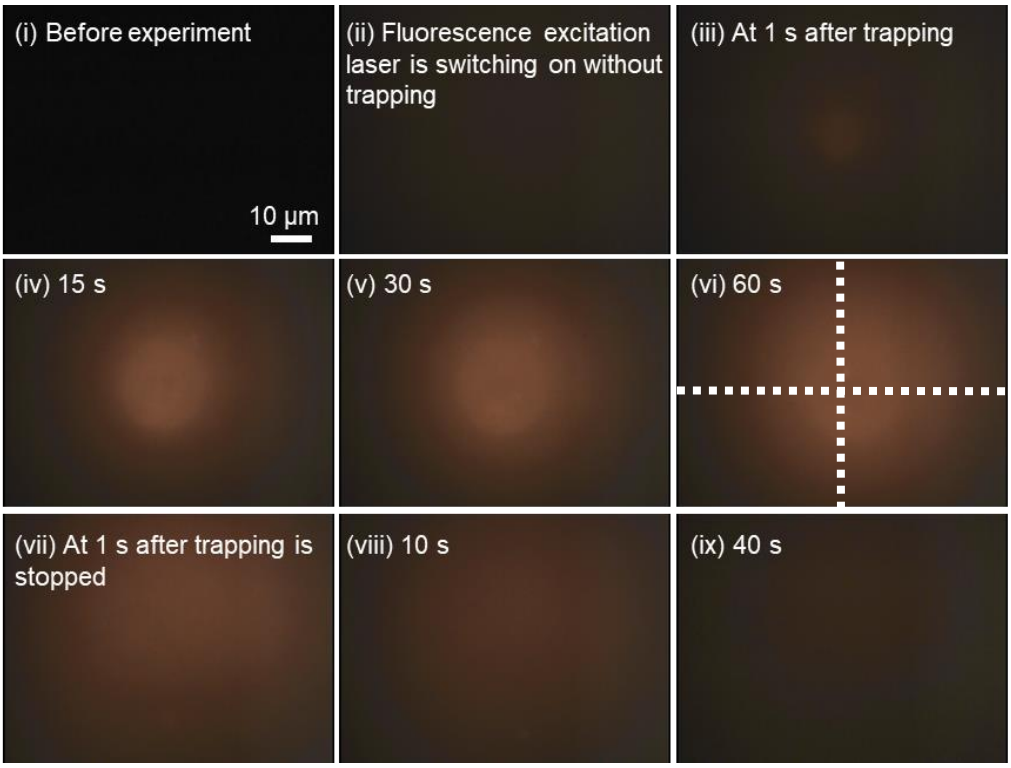

Figure 3.2 Fluorescence images of optical trapping-induced formation of lysozyme assembly observed at D2O solution surface of 26 mM lysozyme, containing RhB-lysozyme with its ratio to lysozyme of 1 to 10000. (i) Before switching on both fluorescence excitation and trapping lasers, (ii)− (ix) after tuning on the fluorescence excitation laser and (vii)−(ix) after switching off the trapping laser. The scale bar is an inset in (i). The white cursor in (vi) is for the analysis of intensity distribution.

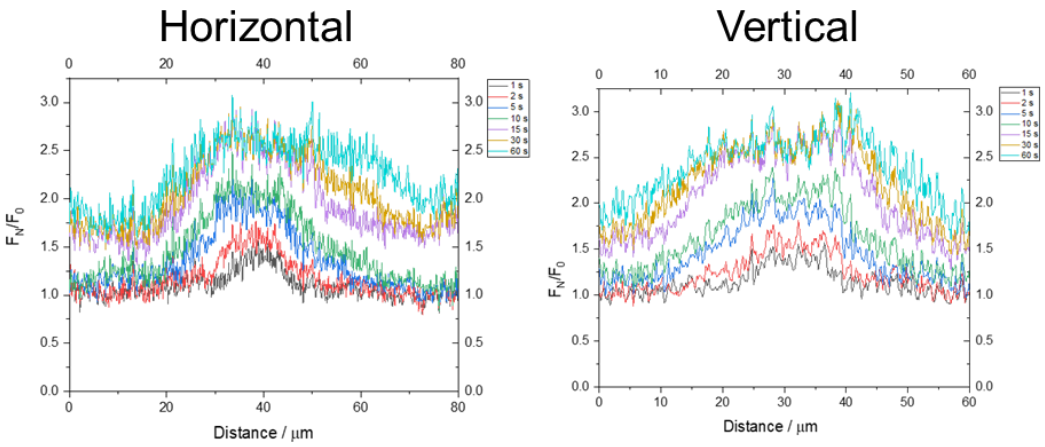

Figure 3.3 Horizontal and vertical fluorescence intensity distribution in the fluorescence image

with the irradiation time dependence. The spatial location is corresponding to the white cursors in Figure 3.2 (vi)

3.3 Raman microspectroscopy

Raman scattering spectra of lysozyme measured before, during, and after the optical trapping were measured at the solution surface, which also supports our idea of optical evolved assembling. The measurement was carried out at the focus and at the position of the lateral distance 40 μm far from the focus. The results are summarized in **Figure 3.4.** The Raman spectrum before the trapping laser irradiation gave the peaks characteristic of lysozyme and increased its intensity with the trapping laser irradiation. After switching off the trapping laser irradiation, the spectrum reverted to the original. These results, including temporal change at the focus, are given in **Figure 3.4 (A)**. A similar spectral change was measured at the position of 40 μm apart from the focal point, as in **Figure 3.4 (B)**. Although the lysozyme concentration of the mother solution was high, optical trapping increased its concentration further, and after switching off the laser, the protein dispersed again, recovering the original concentration. Raman scattering spectra inside the bulk solution and at the air/solution interface were measured and compared with each other in **Figure 3.4 (C)**. The Raman spectrum peaks at 755, 1657, 1553, 1455, 1334, 1006, and 933 cm^{-1} are assigned to symmetric benzene/pyrrole, amide group, tryptophan group, amide group, deformation motion of −CH2− and −CH3 groups, phenylalanine group, and a backbone N−Cα−C stretching vibration of α-helix secondary structures, respectively [38] **Figure 3.5**. Even at 40 μm from the focus, lysozyme was gathered and dispersed with and without laser irradiation, respectively. It was reported that lysozyme adsorbed at the surface undergoes denaturation [39], and this possibility can be checked by the

broadening of the 755 cm−1 Raman band [40]. We doubted whether the denaturation is induced upon the optical trapping, as the unique assembly of lysozyme is grown by irradiating the solution surface. We measured this band at the surface after 70 s irradiation and compared that obtained for the bulk solution. No large difference (i.e., no peak shift and band broadening) was found **Figure 3.6**, so that we consider the denaturated lysozyme must be limited at the surface, although it may have some role at the initial stage of the assembling formation.

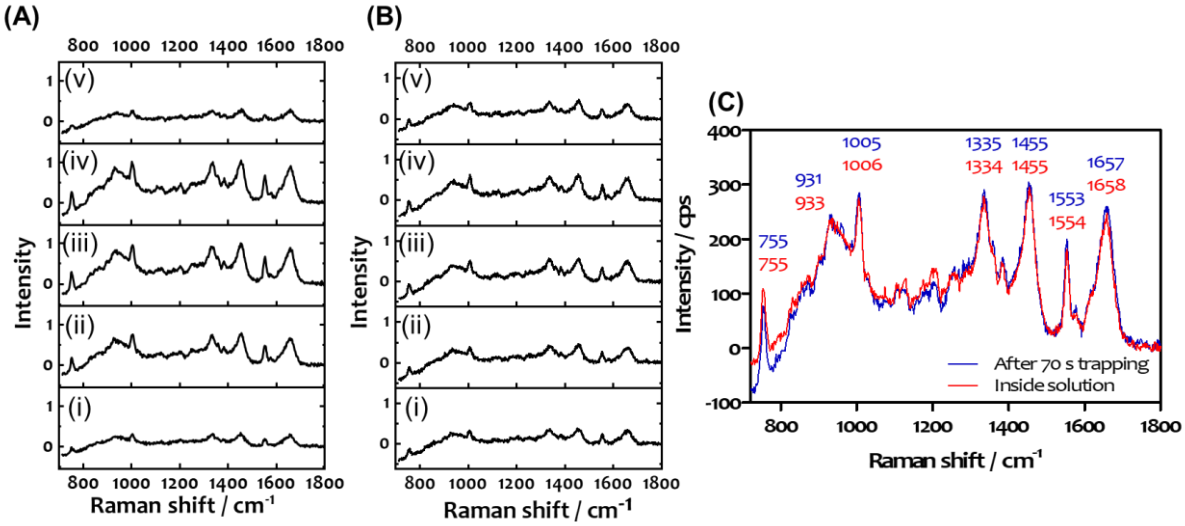

Figure 3.4 Raman scattering spectra of optical trapping-induced formation of lysozyme assembly measured at the D2O surface of 26 mM lysozyme. (A) The spectra at the focal position of the trapping laser. (B) The spectra at 40 µm away from the focus. (i) Before trapping, (ii) at 20, (iii) 40, and (iv) 60 s after switching on the trapping laser, and (v) at 60 s after switching offthe trapping laser. (C) Raman spectra measured at the solution surface after 70 s trapping (in blue) and inside the solution before trapping (in red).

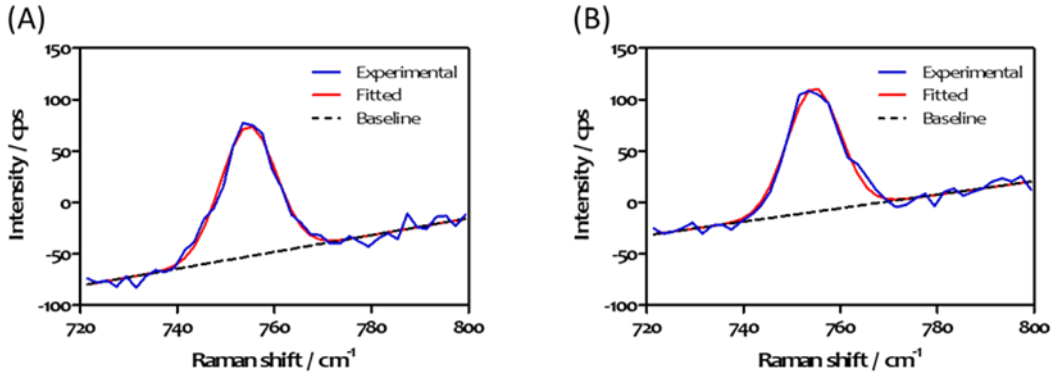

(C)

Fitted parameters	After 70 s trapping	Bulk solution
Pre-exponential	127 cps	121 cps
Mean	755 cm^{-1}	755 cm^{-1}
SD	5.7 cm^{-1}	5.5 cm^{-1}

Figure 3.5 Raman spectrum of the tryptophan band (symmetric benzene/pyrrole in phase) of lysozyme. (A): At the surface after 70 s irradiation. (B): In bulk solution before irradiation. The blue line corresponds to the registered experimental spectrum. The red line corresponds to the fit of a Gaussian function for the tryptophan band. The black dashed line corresponds to the baseline correction. (C): Fitted parameters for panels (A) and (B).

Molecular group	Peak frequency (Experimental) (cm^{-1})	Peak frequency (Reference) (cm^{-1})	Assignment
Tryptophan ring	755	758	Symmetric benzene/pyrrole in phase
N – Cα – C	933	933	ν(N – Cα – C)
Phenylalanine ring	1006	1003	Benzene ring breathing
Amide group	1334	1336	Amide III mode
Methyl groups	1455	1458	Deformation vibration of methyl groups ,$\delta(CH_3)$
Tryptophan ring	1553	1552	ν(C2 = C3),W3 mode
Amide group	1657	1661	Amide I mode

Figure 3.6 Experimental and bibliographic reference 1,2 peaks of lysozyme Raman spectrum. Each peak is assigned to its corresponding molecular group and the vibrational mode according to references [38,40]**.**

Apart from the position where is the laser focus and 40 μm away from the laser focus, dependence of distance to trapping laser focal point with Raman spectra intensity was confirmed. In the case of the measured position is overlapped with trapping laser focal

point, as shown in **Figure 3.7**, from the bottom to the top of the column individually represent the Raman spectrum is, before trapping irradiation, every 20 sec after irradiation, and every 20 sec after trapping laser is switching off. The marked green area in the spectra shows the -CH band which increases comparably after trapping laser is switching on and gradually decreases after trapping laser is switched off. The upper right figure illustrates the procedure of this position dependence experiment. The experiments of distance of 5, 10, 20, 40 are separately repeated to be plotted in the right lower of **Figure 3.7** by integrating the green area. If the Raman spectra is corrected linear to the lysozyme concentration, the result is found that the concentration increases up to 3.7 times surprisingly, that is, about 1400 mg/mL. Besides, Raman spectra intensity increases not only inside, but also outside of the domain, suggesting that concentration is increased regardless of the position only with different enhancement ratio. Lastly, the concentration distribution from trapping laser focus to outside displays a gradient in a radial fashion. We assumed the edge of the domain arises from the concentration difference as mentioned in **section 3.1**; however, the results of Raman measurements do not show any significant gap between inside and outside of the domain, ruling out this possibility. To assure the reliability of the result of -CH band, we also analyzed other band area such as the wavenumber of 1300-1400 cm^{-1} (amide group), 1400-1500 cm^{-1}(methyl group), 1500-1600 cm^{-1} (tryptophan ring), and 2400-2500 cm^{-1} (D_2O band) (**Figure 3.8**). Except the D_2O band, the other 3 regions of the wavenumber all show the enhancement facto of about 3.5 that is similar to the result of -CH band. Therefore, we consider the result is reliable. Furthermore, the experiment of lysozyme concentration dependence with Raman spectra intensity shows a clear linearity (**Figure 3.9**). Of note, the linearity of the lysozyme concentration within the concentration of 400 mg/mL. It is hardly possible to

prepare more concentrated lysozyme solution in conventional methods. Nevertheless, optical trapping enables the supersaturation of lysozyme solution prepared. Despite the demonstrated linearity, the Raman spectra intensity from our result may not completely suggest the increment of lysozyme solution.

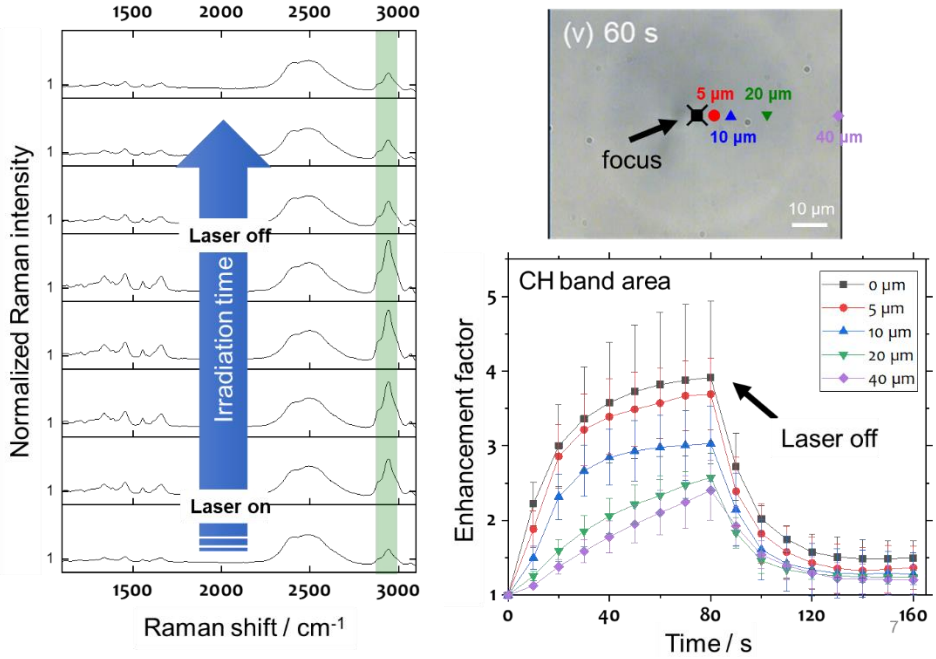

Figure 3.7 Left: bottom is the spectrum that is measured before trapping laser is turned on. Each vertical column is after the illumination of trapping laser for 20 second. The green bar is the region that integrated in the right lower figure. The right upper: illustration of the measured position for the Raman measurement. The right lower: the integration of CH band as the function of trapping laser irradiation time. Enhancement factor represents the intensity compare to before trapping laser is turned on. The color of the curve corresponds to the color in right upper figure.

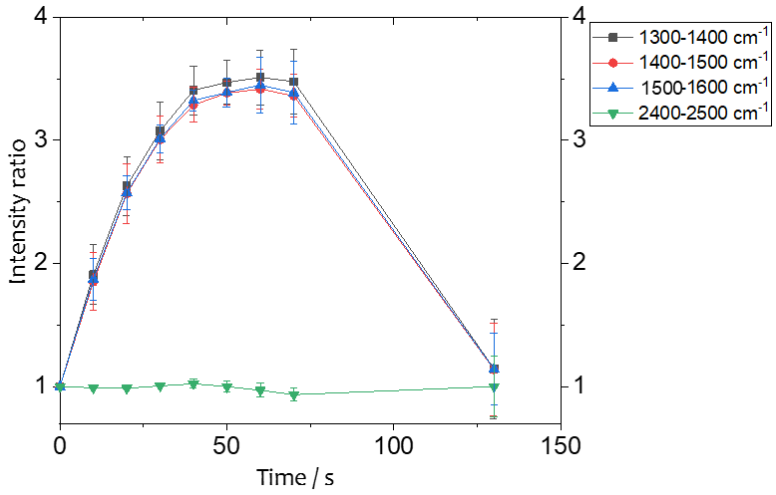

Figure 3.8 The integration of each region (different color) divided by the integration of before trapping laser is turned on, as the function of trapping laser irradiation time.

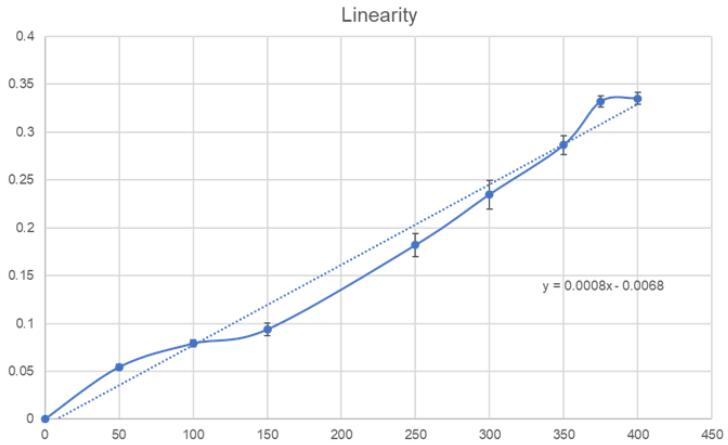

Figure 3.9 The linearity of Raman spectrum intensity to the series concentration of lysozyme solution. Horizontal axis: Lysozyme concentration. Vertical axis: Raman spectrum intensity with the arbitrary unit.

3.4 Three-dimensional structure of lysozyme assembly

Since our optical microscope system only gives conventional two-dimensional information on the dynamics at the focal plane, but it is important to judge to what depth the MPs are transported below the solution surface. This was made possible by observing the transmission point spread function (PSF) for each individual PS MP and considering

the refractive index difference among air, D_2O and lysozyme solutions. Below figure shows the PSF profile at different imaging depths for a single 1 μm PS MPs in D_2O. Based on the judging focused and defocused pattern of the PS MPs, suggesting the assembly of PS MPs grows three-dimensionally during the trapping laser irradiation. As the assembly of PS MPs is used as the indicator for the deduction of lysozyme assembly. Therefore, the standard of the judgement for the particle location corresponding to the observing plane is a critical demand.

3.4.1 Depth definition by polystyrene microparticle in the transmission image

As shown in **Figure 3.10**, a series of transmission images of 3 for a single 1 μm PS MP in D2O with different depth of observing plane. In the series of images, the single PS MP is located at the solution surface due to the buoyance, meanwhile, the objective lens is moving upward and downward to record the images, taking into account the relative position of the solution surface. The objective lens is computer-controlled whose precision can reach to the level within 0.5 μm. The recorded position series of transmission images were started from above to the solution surface 5 μm, following with moving downward of the objective lens every 2 μm including the location of solution surface where is defined by an indicator laser with the tightest focal point pattern. The definition process must encounter one issue, refractive index mismatch, leading to misjudge of the realistic observed-plane for our sample. As shown in **Figure 3.11** [41], the displacement of objective lens is denoted as Δz, and the displacement of observing plane in the solution is Δr. In the case of $n_1 > n_2$, the refractive index mismatch will cause $\Delta z > \Delta r$; however, in our experimental condition, objective lens is manipulated in the air

($n_1 \approx 1$) which is smaller than the sample solution, D_2O ($n_2 \approx 1.33$), thus, the $\Delta r > \Delta z$. The correlation scale to modify this mismatch is about 1.46 which is determined by the measurement of the height between two cover glass with a center-hollowed spacer in the middle. First measurement, there is only air filled in the center of the spacer, that is, the $\Delta z = \Delta r$. The distance between two glass is measured, 117 μm which is also a displacement of the objective lens. Secondly, the D_2O is filled int the spaced between two glass, that is same condition as our experiment. The distance between two glass in theory is 117 μm, nevertheless, the displacement of the objective lens is about 80 μm. In average, every 1 μm displacement of objective lens in the air, suggesting the displacement of 1.46 ($\frac{100}{68}$) μm in the solution. In our experiment, the objective lens is moving downward 1, 3, and 5 μm below the solution. Consider the correlation scale to modify, the practical displacement of the observing plane in the D_2O solution actually is, 1.5, 4.4, and 7.3 μm. It is clear showing in the **Figure 3.10**, the observation focal plane was set at (i) +5, (ii) +3, (iii) +1, (iv) 0, (iv) −1.5, (v) −4.4, and (vi) −7.3 μm above (+) and below (−) the solution surface. The scale bar is inserted in the last photo. Through this assistance of the judgement, we can recognize the relative position between PS MPs and observing plane.

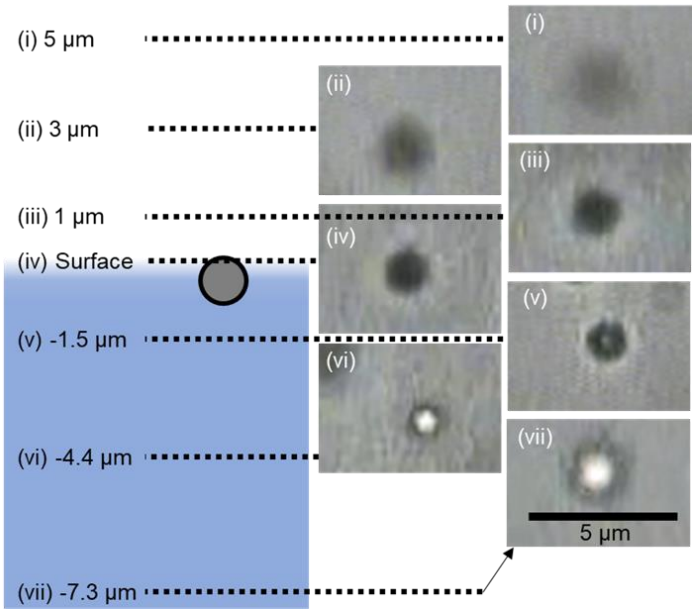

Figure 3.10 Transmission images of 1 µm PS MP located at the solution surface observed at different depth. The observation focal plane was set at (i) +5, (ii) +3, (iii) +1, (iv) 0, (iv) −1.5, (v) −4.4, and (vi) −7.3 µm above (+) and below (−) the solution surface. The scale bar is inserted in the last photo.

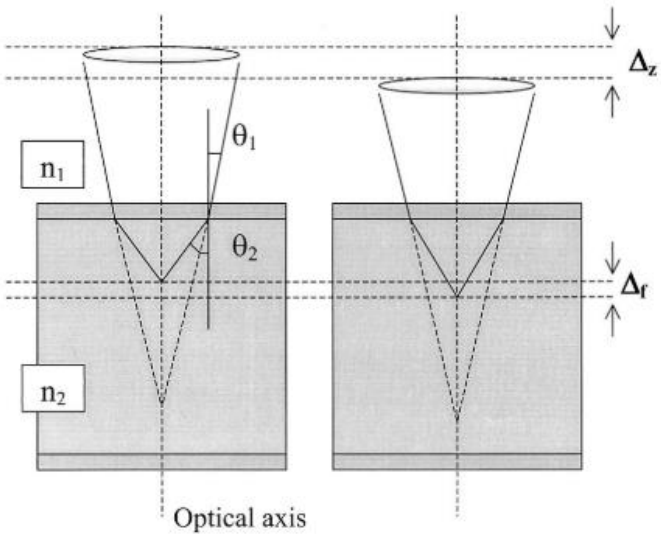

Figure 3.11 Illustration of encountering the refractive index mismatch problem when focusing the laser in a medium through an objective lens [41].

3.4.2 Cooperative optical trapping of polystyrene microparticle and lysozyme

Optical trapping of PS MPs at solution surface has been systematically carried out in our laboratory. One of the distinctive results is on the assembling, pistol-like ejection, and rearrangement of 1 μm PS MPs at D_2O solution surface [18]. Herein, we re-examined this behavior by focusing the laser to the surface of D_2O and lysozyme solutions. As shown in **Figure 3.12 (A)**, many PS MPs showed a variety of apparent size and darkness, which is comparably indicates different depth. As the density of PS MP is lower than that of D_2O, the MP is located at D_2O solution surface exposing a few portions of its total volume to air. Thus, we could know how the transmission PSF changes along with their relative height position above and below the imaging plane. As shown in **Figure 3.10**, the single MP looked dark when the imaging plane was set at the surface and became more defocused when the plane was above the surface. On the other hand, when the plane was adjusted to be 1.5 μm below the surface, the MP image is still black. Notably, it looked white with a dark ring as the plane was shifted further below. Thus, the MPs, which looked clearly black, should be located near the surface, while the more blurred MPs were located much below the surface. Therefore, we conclude that the individually visible MPs were located near the surface layer with a thickness of about 5 μm. Upon switching on the trapping laser, the PS MPs were gathered at the focus and formed a disk-like assembly with the diameter of about 8 μm. The assembly seemed at the surface as all MPs are black.

In the case of 20 mM lysozyme D_2O solution, the visible MPs were limited and some of them formed aggregates as **Figure 3.12**, meaning that most of PS MPs are distributed not in the surface layer of about 5 μm thickness. It is considered that the surface layer is occupied by lysozyme, leading to PS MPs are unattainable of the surface, although the

density of PS MPs (1.05 g/mL) is smaller than those of D_2O (1.11 g/mL) and D_2O solution of 20 mM lysozyme. The distribution change of the 1 μm PS MP from **Figure 3.12 (A)** to **Figure 3.12 (B)** suggests that a lysozyme layer is prepared at and below the surface, and the MPs cannot be distributed there. Such a lysozyme layer has never been reported as far as we know, but it is recently reported that sunflower protein gives a film with a thickness of 130 nm [42], suggesting the film formation is possible. With the 10 s irradiation of the trapping laser, we could see that a PS MP disk-like assembly was prepared, being coupled with some linearly ejected aggregates of MPs. This behavior, which is similar to that of 1 μm PS MPs in D_2O [18], should occur at the lysozyme layer with the thickness of a few μm. Their movement was slower than that of case for 1 μm PS MPs in D_2O, the ejected distance was shorter, and the ejected aggregates were not dissociating and not dispersing fully to the surrounding, which can be ascribed to a higher viscosity of the protein solution compared to D_2O. This interpretation is consistent with the theoretical work introduced below [43], that is, lysozyme solution becomes rigid and like a frozen state above the concentration of 20 mM.

When the lysozyme concentration was further increased to 26 mM, an exclusively different assembling behavior was observed. As shown in **Figure 3.12 (C)**, the 1 μm PS MPs form a linear assembly, and it elongated with the irradiation time. The apparent length reached close to 30 μm after 80 s irradiation, while it became thicker and more blurred from the tip to the focal point. Namely, it is not a chain of single PS MPs, but more MPs are involved in forming the assembly, particularly at the position close to the focus. The clearness in the assembly image depended on the position with respect to the focus, meaning that the formed aggregate is vertically tilted. Even the tip of the linear assembly was identified to be located below the surface; many MPs in the central part

were observed lower, and the end of the assembly was at a even deeper position. This is judged by comparing the PSF of each individual MP with those in (**Figure 3.10**). In this experiment, the polarization direction dependence was not observed. The linear assembly formation was not arranged using a laser power of 0.5 W, so the laser power was kept to 1.0 W through all measurements. We saw a slight bright ring-like pattern with a dark domain in its inside after 80 s of irradiation. The white ring must be due to the refractive index difference between the solutions inside and outside the ring. The trapping focal area is about 1 μm, so that only a few MPs are directly irradiated, while a long linear assembly of a few tens of μm is prepared in the nonirradiated area. Upon switching off the trapping laser, the linear assembly slowly sank down with a speed of about 0.5 μm/s and dissociated to individual MPs after the dark domain disappeared completely. It is worth noting that optical assembling dynamics of the 1μm PS MPs was completely changed by increasing the lysozyme concentration from 20 (300 mg/mL) to 26 mM (375 mg/mL). As mentioned above, the supersaturation is observed at 366 ± 10 mg/mL, while Baumketner and Cai reported that lysozyme clusters are rigid and almost frozen for the concentration of 300 mg/mL [43]. Their theoretical consideration is based on the model that the interaction potential between lysozyme is repulsive everywhere except at a short distance. They predicted that small and extended clusters of lysozyme are prepared at low concentration, and large clusters are generated and collapsed with each other at high concentration. Our experimental result shows that the optically gathered PS MPs cannot enter the collapsed clusters and, once a single MP goes to the edge of the domain, other MPs follow it. Our understanding seems well supported by this theoretical study.

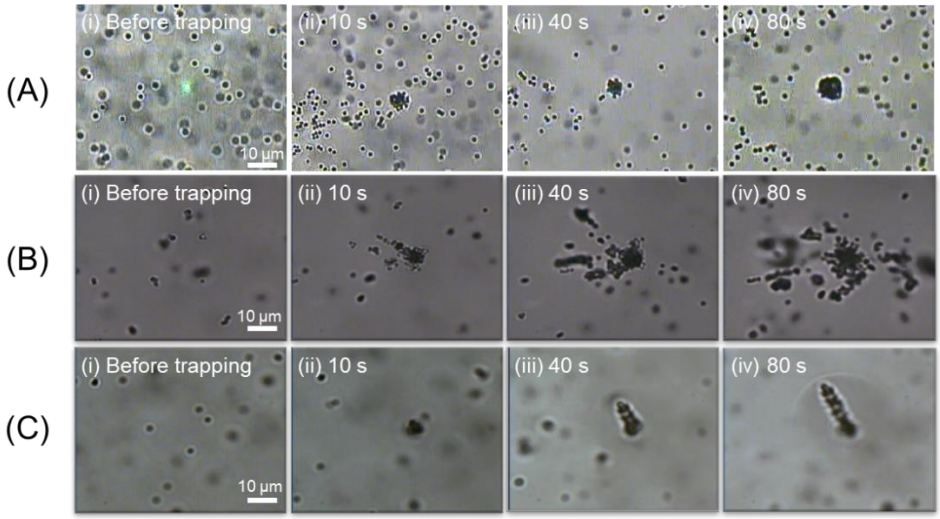

Figure 3.12 Transmission images of optical trapping-induced formation of a single assembly of 1 μm PS MPs at solution surface: (A) D2O; (B) D2O solution of 20 mM lysozyme; (C) D2O solution of 26 mM lysozyme. (i) Before trapping and (ii)−(iv) after switching on the 1064 nm laser. The scale bar is an inset in (i)

To examine whether this linear assembly formation is a general trapping behavior or not, we studied PS MPs with a diameter of 0.75, 3, 4.5, 6, and 10 μm in addition to that of 1 μm. The results are summarized in **Figure 3.13 (A)**, where lysozyme concentration was prepared at 26 mM, the same laser power of 1 W was always applied, and the irradiation time was 3 min. It is unexpected to see that, although the focus area is about 1 μm^2, some linear assemblies reach a submillimeter length. The maximum length of the linear assembly of the PS MP is 25, 34, 105, 110, and 102 μm for the diameter of 0.75, 1, 3, 4.5, and 6 μm, respectively. In the case of the 10 μm PS MP, the linear assembly was not observed. Always one linear assembly is formed, except the latter MP, and its generation behavior is reproducible, although the length and the shape fluctuate from experiment to experiment. The averaged length is given as a function of the MP size in **Figure 3.13 (B)**. If the MP size is larger, the induced optical force is stronger, giving a longer assembly. On the other hand, the elongation of the larger MPs may be more resisted

by a viscous and dense lysozyme layer and solution, compensating the optical pushing force. Thus, the size dependence has a saturation tendency, giving a peak due to the competition between these two forces.

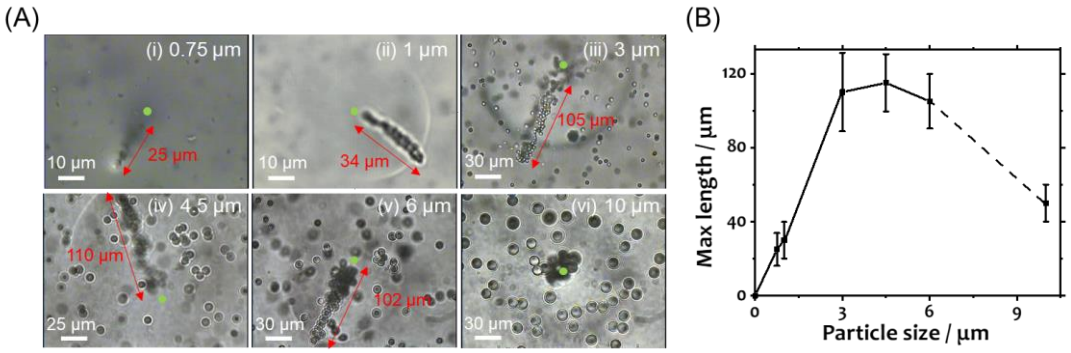

Figure 3.13 (A) Transmission images of optical trapping-induced formation of a single assembly at the D2O solution surface of 26 mM lysozyme. The maximum length of PS MPs is given in (i)−(vi), which were obtained at 70, 120, 350, 100, 140, and 210 s after switching on the 1064 nm laser, respectively. The scale bar is an inset in each photo, while the focal position is marked by a light green spot. (B) The maximum length of the prepared linear assembly as a function of the size of PS MPs. As the 10 μm PS MPs did not give a linear assembly, it is connected to others by a dash line.

3.4.3 Determination of the lysozyme assembly structure

As we used a conventional optical microscope, we could only acquire lateral images. Thus, we shifted the focal plane, and observed the trapped PS MPs at lower depth positions soon after stopped the irradiation at the surface after a certain trapping time. Here, 3 μm PS MPs were chosen as the indicator, as the transmitted PSF is better resolved than that of 1 μm MPs. We could determine the depth of each part of the linear assembly, and this depth assignment has enabled us to get a three-dimensional (3D) morphology of the linear assembly. First, we focused the trapping observation plane at the solution surface to prepare a single linear assembly of the PS MPs by irradiating the trapping laser

for 300 s. All the MPs are always defocused and look black (**Figure 3.14 (A-i)**), indicating that all the MPs are localized much below the surface. Second, the elongated assembly still stayed there for a while even though the trapping laser was switched off, and a disk with a dark edge of a few tens μm diameter appeared in **Figure 3.14 (A)**. This would be a shrunken assembly of lysozyme, suggesting that it stays transient without optical trapping.

This morphology observation of the linear assembly was carried out by shifting the focal plane and recorded. Some representative frames are selected and listed in **Figure 3.14**. By shifting down the focal plane by 6 μm, we found the PS MPs at the tip of the linear assembly in **Figure 3.14 (A-ii)** were better focused compared to **Figure 3.14 (A-i)**. This height shift of 6 μm in the solution was achieved by mechanically driving the objective lens by 4 μm, considering optical mismatching (as the objective lens was in air, while the focus is inside the D_2O solution of lysozyme) [44]. Further shifting down the observation plane, most well focused PS MPs were not at the top of the linear assembly, but MPs in more of the inner portion of the assembly were clearly observed. This understanding is obtained from **Figure 3.14** (**(A) iii-vi)**, where well focused PS MPs were obtained at the depth of 12, through 17 and 23, and to 29 μm, respectively. This z-stack enabled us to understand the 3D morphology of the linear assembly of PS MPs, which is shown in **Figure 3.14 (B)**. Here, the electric field intensity distribution of the 1064 nm trapping beam was calculated for neat D_2O and overlapped with the 3D morphology of the linear assembly of PS MPs. The calculated electric field does not show a Gaussian distribution because a high NA objective lens is used and some stepwise intensity distribution was observed. Moreover, since the assembling of lysozyme changes the refractive index and dielectric constant, the electric field is modified from time to time.

All these changes in refractive index and dielectric constant are not considered here.

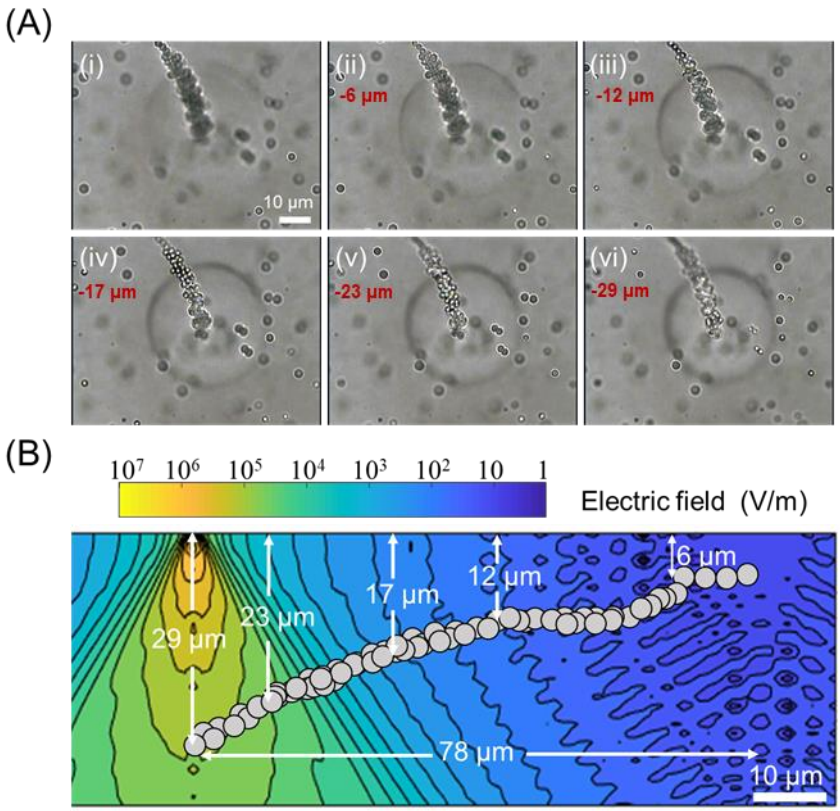

Figure 3.14 (A) Transmission images of the single assembly of 3 μmPS MPs observed at different depths in a D2O solution of 26 mM lysozyme. Images (i)−(vi) were obtained at 0, 0.33, 0.66, 0.93, 1.26, and 1.59 s after switching off the 1064 nm laser, where the depth is calculated to be at 0, 6, 12, 17, 23, and 29 μm below the surface, respectively. The scale bar is an inset in (i). (B) The 3D long linear assembly of 3 μm PS MPs is deduced and overlaid on the electric field intensity distribution of the focused 1064 nm trapping laser. The intensity distribution was calculated with angular spectrum representation, and displayed in a logarithm scale.

3.4.4 Mechanism of the cooperative optically evolved assembling

It is interesting to note that the assembly elongated continuously from the center to the upper right without folding and bending. Here, we describe the possible dynamics and mechanism of the linear assembly formation. As PS MPs are lighter than lysozyme

solution, the buoyance force should push them toward the surface. However, the observation of small 0.75 and 1 μm PS MPs does not support this expectation as shown in **Figure 3.13 (i, ii)**. Lysozyme was densely populated at and near the surface and did not allow individual MPs to enter the lysozyme layer. The buoyance of those small MPs may be not enough to push them to the surface. Optical trapping attracted sequentially PS MPs and they were coming to the position just below the focus as the trapping laser intensity was still high there. Initially, the elongation direction was observed to be random because the elongation direction seemed different from experiment to experiment. We clarify the elongation direction by illuminating the trapping laser at different positions with same distance to the topmost position of the surface in a radial fashion. As a result, the elongation direction is always extending along the topmost position of the surface, namely, the elongation direction has symmetrical dependence to the topmost position of the surface. Based on the results we clarify what geometrical, optical, and chemical conditions are responsible to determine the length of the elongation of the linear assembly.

The first PS MP is pushed up by the optical force and reaches a region where the MP cannot penetrate because there the highly concentrated lysozyme forms rigid collapsed clusters. Then, the MP will follow the direction where the buoyance force is larger. The trapping laser will push more MPs toward the lysozyme domain. When a second MP arrives there, the first MP will generate an attractive hydrodynamic force on the second MP. At this moment, the second MP is simultaneously experiencing both buoyancy and hydrodynamic forces, which push the MP toward the direction of the first MP. This trapping and position shift events were repeated many times, forming a linear aggregate. It is worth noting that lysozyme trapping also proceeded simultaneously during the laser irradiation, making its layer thicker, wider, and more concentrated by sequential

assembling the collapsed clusters. Thus, the later coming PS MPs were collected further below the focus and pushed to follow the elongating linear aggregate. We should remember that large and dense lysozyme assembly and PS MPs are both hydrophobic, and electrostatic interactions between them are effective, so they are stably adhered with each other, as long as the assemblies are kept and do not undergo dispersion.

The growing processes of the linear assembly are illustrated in **Figure 3.15**. Initially, lysozyme concentration is over the supersaturation (shown in yellow color), resulting in the formation of its layer with the thickness of a few μm (in orange-yellow). Upon switching the trapping laser on, both MPs and lysozyme are attracted to the focus. As lysozyme is homogeneously distributed, it is attracted first before the PS MPs are gathered. The local concentration of lysozyme becomes even higher and its area (in orange color) expands laterally and vertically. Then PS MPs are attracted toward the focal point at the surface, while they do not penetrate into the denser lysozyme assembly. Consequently, they shift as a linear aggregate and grow sequentially, as PS MPs are supplied from the bottom. Optical trapping of lysozyme cooperatively proceeds further, leading to the formation of a more concentrated, wider, and larger assembly probably consisting of collapsed clusters. In the **Figure 3.15**, the dotted lines in the assembly (in orange color) represent a possible border between two concentration areas; the central part at 300 s after the trapping was started has the highest concentration, and outer is lowest, but still higher than 26 mM.

After switching off the trapping laser, the black ring came from the outside and shrank to the present size, which was clear in **Figure 3.14 A(iii)−(vi)**. This ring should correspond to a white ring in **Figure 3.12 C (iv)**, where the difference in the dark and white in images is well explained with the relative vertical position of the objective lens

and the target. There might be a concentration gap, or different phase between the mother solution (outside) and the trapped concentrated region (inside), thereby the refractive index change. It is interesting to note that the radius of the black ring is smaller than the linear assembly here, while both ring and assembly seemed stable during this observation. Some MPs were located or adsorbed at the ring, suggesting that MPs are stabilized at the interface between the mother solution (outside) and the trapped concentrated region. This is consistent with our idea that the linear assembly is prepared along the lysozyme assembly.

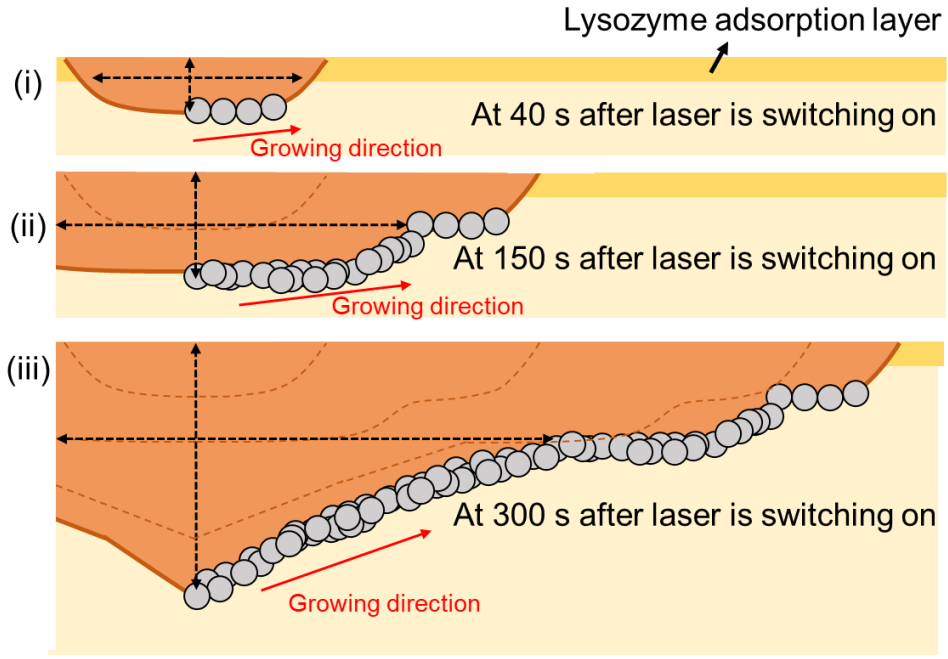

Figure 3.15 Schematic illustrations representing how the linear assembly grew along the lysozyme assembly. Lysozyme adsorption layer is formed before introducing trapping laser. Lysozyme assembly is formed from the trapping laser focus and growing laterally and axially, indicating in the dark orange area. Linear assembly of polystyrene microparticles is growing toward the direction, indicating by the red arrow.

3.5 Summary

We have demonstrated optical trapping could not only manipulate the single particle but also assemble the them to the laser focal point. In the case that trapping laser focus is set at the interface, e.g. solution surface, the assembly can expand to outside of the laser focal area and eventually larger than 100 μm. Fluorescence imaging and Raman microspectroscopy are applied for the confirmation of this lysozyme molecules behavior under optical force. We clearly point out that lysozyme assembly expands outside from the laser focal point and whose concentration increases as a function of the trapping laser irradiation time. To overcome the problem of colorless lysozyme molecules under microscope, PS MPs are added to characterize and monitor the three-dimensional expanding process of lysozyme assembly as an indicator. By judging the clearness of the PS MPs in the solution, the height of the assembly is possibly estimated.

Chapter 4 Two-stage optical trapping behavior of lysozyme assembling

Optical trapping at interfaces has recently gained relevance due to the expansion of optical potential far away from the focus, especially for protein where submillimeter structures have been described as mentioned the **Chapter 3**. In this chapter, the initial state of lysozyme clusters at the surface and will it evolve with the irradiation time is discussed. Nonetheless, the concentration dependence reveals the dynamics of how lysozyme clusters inside solution are collected and transported toward the focus, which eventually results to a border between mother solution and the collected clusters, although no concentration gap is detected. This two-stage optical trapping occurs due to long-range interaction originating from the focus.

4.1 Temporal evolution of transmission and fluorescence images

To monitor the concentration enhancement factor (EF) of lysozyme solution due to the trapping effect, two synchronized CMOS cameras were used to acquire the transmission and fluorescence images at 645~705 nm and 520~620 nm, respectively as shown in **Figure 2.11**. Same as the fluorescence imaging experiment done in Chapter 3.2, the RhB-lysozyme is used for this synchronized imaging experiment. The ration is also same as the previous, 1:10000 (RhB-lysozyme to the hen egg white lysozyme). Again, D_2O is used as a solvent, since its temperature elevation due to the 1064 nm laser absorption is reduced to one tenth of that in H_2O (23 K/W).

Figure 4.1(a) and (b) show the transmission and the fluorescence temporal evolution of a 375 mg/mL lysozyme solution after switching on the trapping laser. Of

note, this concentration is slightly over the saturation concentration (366 mg/mL) [33]. In the transmission images, a dark area appears at the focus and expands to the outside after switching on the trapping laser. The area is surrounded by a little bright “ring”, which is approximated with the dotted red circle. Meanwhile, the trapping laser irradiation leads to fluorescence increase in a circular area of a few ten micrometers, much wider than the trapping focus (approx. 1.5 μm). To correlate both images, the dotted red circle is overlaid on the fluorescence image (**Figure 4.1 (b)**). Temporal change in the fluorescence image is analyzed by defining fluorescence intensity EF, meaning the calculated ratio of fluorescence intensity integrated in the circle area (**Figure 4.1 (c)**) at a given time to that before irradiation. Since the RhB-lysozyme fluorescence signal is confirmed to be linear with its concentration (as shown in **Figure 2.7**), the EF represents how many times lysozyme concentration is increased.

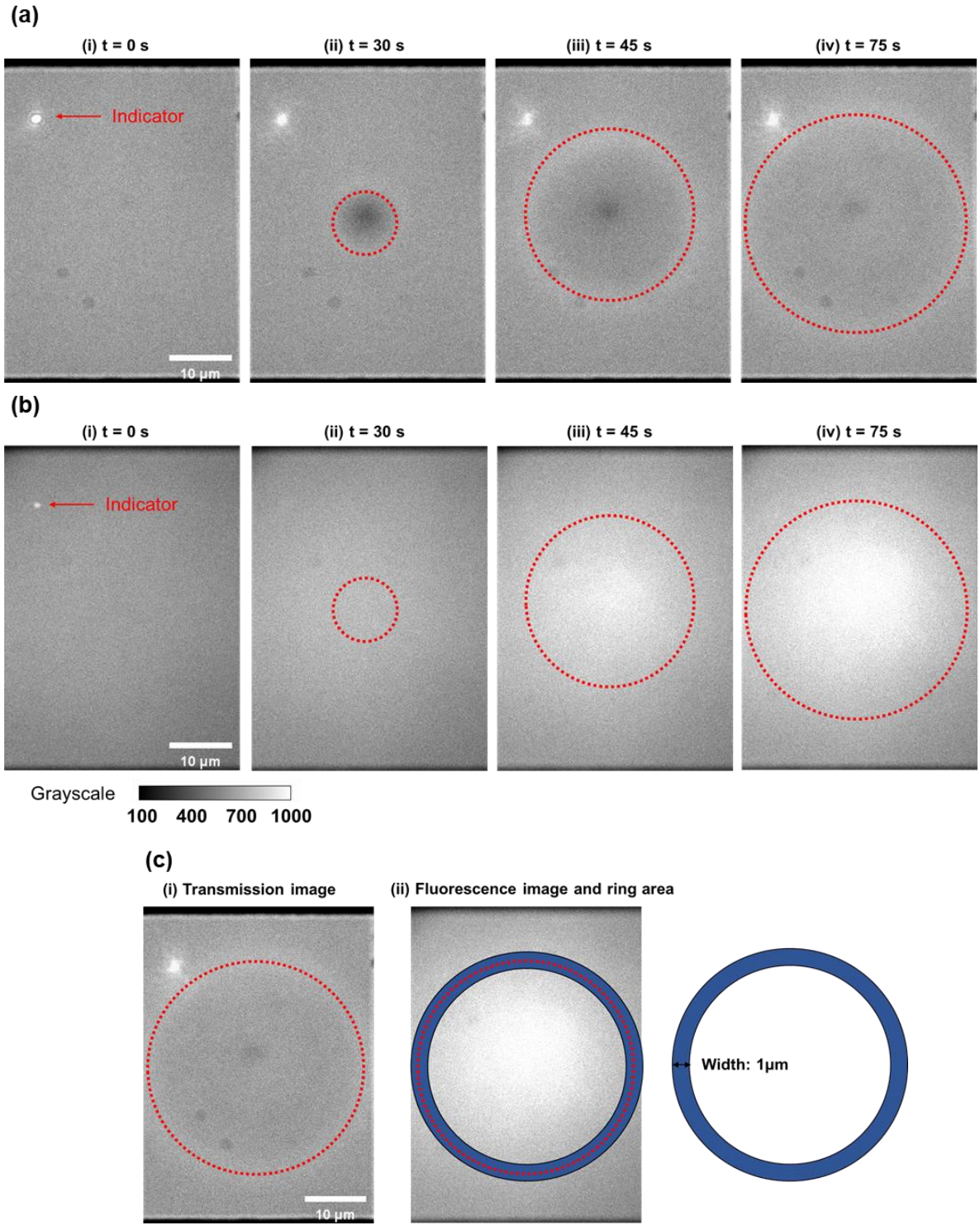

Figure 4.1 (a) Transmission images observed at the surface of the 375 mg/mL D2O solution lysozyme. (i) Before irradiation. (ii)-(iv) After switching on the trapping laser of 0.6 W. An upper left bright spot is caused by a 640 nm indicator laser used to monitor the surface position. As a

visual aid, the contrast of the images is enhanced to clearly observe the white "ring", whose centers are represented with dotted red circles. (b) Synchronous fluorescence images. The dotted red circles are overlaid. (c) The width of 1 μm is given to the dotted circle, which gives the blue ring area. Its fluorescence intensity at different diameter is compared to that of variable irradiation time of the trapping laser, which is defined as fluorescence "enhancement factor".

4.2 Power dependence

First, the EF at the focus is examined for different trapping laser power using the 375 mg/mL solution (**Figure 4.2**). While the EF does not appreciable increase for 0.1 and 0.2 W, it reaches a value of around 2 (initial concentration is doubled, that is, 750 mg/mL.) before 10 min irradiation for 0.4 W. The result at 0.6 W shows a rise soon after the switching on and a relatively gradual increase with the irradiation time, so that this power is used for examining various trapping conditions. In comparison of the results of 0.4 W and 0.6 W, the former one shows the linear trend of increment as the function of the trapping irradiation time; the latter one, on the other hand, seems to reach a plateau at the irradiation time of 3 min. However, the concentration increasing linearly after time of that. We consider the initial enhancement is raised from the trapping force to collect the lysozyme clusters; the subsequent enhancement may be involved in the evaporation effect. As the result, the non-linear increment occurs in the trapping laser irradiation time.

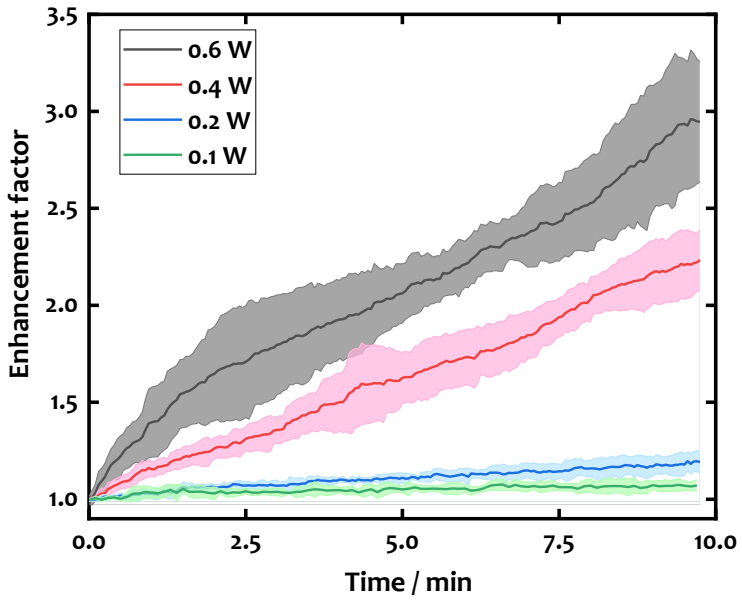

Figure 4.2 Temporal evolution of fluorescence "enhancement factor" with the irradiation time. Trapping laser power dependence of the 375 mg/mL lysozyme solution at the focus.

4.3 Concentration dependence

Next, we study the dependence of EF at the laser focus on the initial lysozyme concentration, fixing the trapping laser power at 0.6 W (**Figure 4.3**). The EF value of the 100 mg/mL solution increases very slowly, while the slow rise of the 200 mg/mL solution is switched to quick one after roughly the irradiation time of 7 min. The switching takes place around EF of 1.5, namely, the concentration of 300 mg/mL is critical for understanding the dynamics and mechanism. In the case of 300 and 375 mg/mL, the EF value rises soon after switching on and reaches 3 at 10 min. The increment trend of 300 and 375 mg/mL are similar to each other, the initial growth rate of 375 mg/mL is higher than 300 mg/mL though. The concentration of 200 and 100 mg/mL possess the initial similar increment trend until the irradiation time of about 5 min, implying the initial concentration plays the essential role for trapping efficiency.

Furthermore, a thick lysozyme layer is formed, and its concentration near the surface

finally reaches around 600 mg/mL even for the 200 mg/mL solution [**Figure 4.3 (b)**]. A small concentration gradient is observed, as the EF slightly decreases with the distance from the focus, which is common through whole irradiation time. After switching off the trapping laser, the concentration starts to decrease at all the positions.

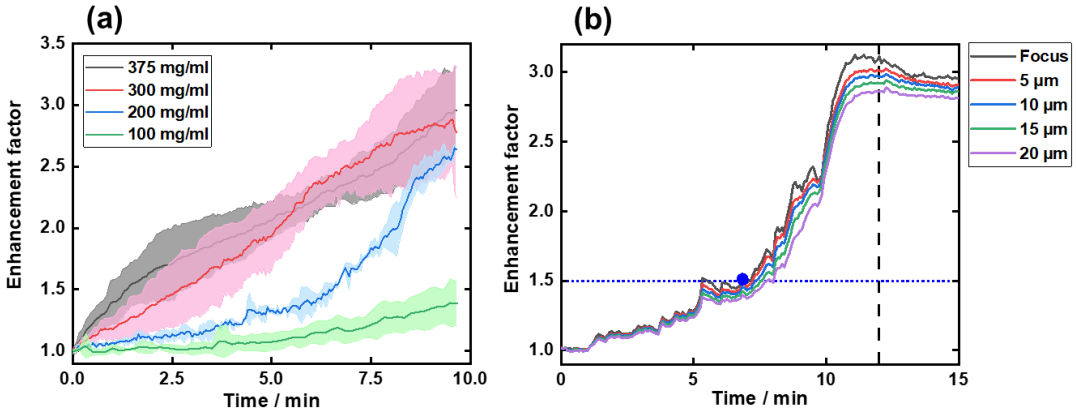

Figure 4.3 Temporal evolution of fluorescence "enhancement factor" with the irradiation time. (a) Lysozyme concentration dependence at the focus with the laser power of 0.6 W. (b) Radial position dependence of the 200 mg/mL lysozyme solution at the laser power of 0.6 W. The blue spot shows the "enhancement factor" when the white "ring" appears, while the dotted line corresponds to the time when the trapping laser is switched off.

4.4 Mechanism of two-stage optical trapping

4.4.1 Spatio-temporal evolution of fluorescence enhancement

To investigate the formation of the white ring, the transmission and fluorescence images are simultaneously acquired and correlated with each other for the 375 mg/mL solution (**Figure 4.4**). Transmission image and the fluorescence imaging were used for checking the expansion of the white ring and enhancement factor (EF) of the concentration. On one hand as expected, the EF value increases not only at the focus but also even at the position far from the focus (~25 μm). On the other hand, the diameter of the white "ring" observed in the transmission images gradually expands (**Figure 4.4**). It is worth noting that the fluorescence intensity inside and outside the "ring" does not show any apparent jump or gap, instead smoothly decreases with the distance at respective irradiation time. We conclude the fluorescence (i.e. the lysozyme concentration) increase is not directly related with the formation of the white "ring".

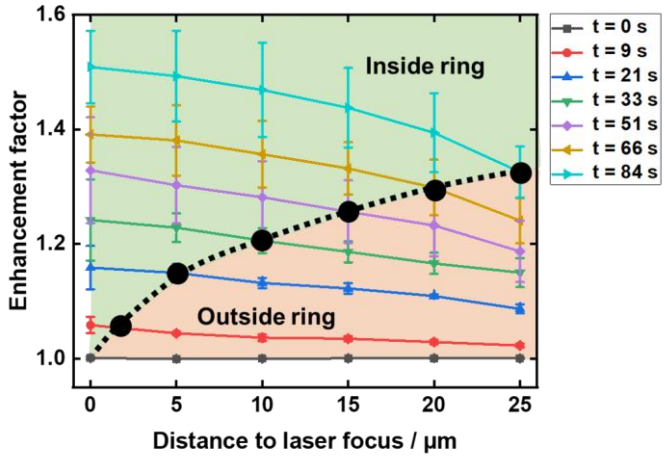

Figure 4.4 Spatio-temporal evolution of the fluorescence "enhancement factor" of the 375 mg/mL lysozyme solution. The black closed circles represent how the white "ring" in the transmission image expands with the irradiation time

4.4.2 Visualization of lysozyme assembly by single micro-particle

To gain further details about the origin of the white "ring", we visualize the present assembling phenomenon of the 375 mg/mL solution by adding PS MPs (**Figure 4.5**). The focus of trapping laser is set to the lysozyme-D_2O solution surface, and the axial position of the MP(s) is estimated by comparing their image clearness with the **Figure 3.10**. Initially, the MP may be under Brownian motion, but it is attracted to the focus upon switching on the laser, giving a clear shape, and stayed there for a while (**Figure 4.5 (b)**). As the refractive index of PS (1.59) is higher than that of the D_2O solution of lysozyme (1.4 measured for the 375 mg/mL solution), this is considered just as a conventional trapping behavior. However, the trapped PS MP is soon de-trapped and starts to move from the focus to the outside (**Figure 4.5 (c)**). A similar behavior before and after switching on the trapping laser is also observed for other PS MPs sizes (1 to 20 μm. The single particle tracking analysis of the first- and second-trapped MPs is performed (**Figure 4.5 (g)-(h)**), where random Brownian motion is not observed due to the high stiffness of the protein layer. The de-trapping behavior means the loaded optical force is overcome by hydrodynamic force due to the further viscous flow in the layer and the decrease in the refractive index difference between the MP and the layer. The second- and third-trapped MPs appear from the bottom of the inside solution, by judging their image clearness, and come to the position below the focus. Then, they shift to the same direction without trapping at the focus. If the MP is laterally away and out of the irradiation cone, as for example, the vague MP at the left side is not attracted to the focus (**Figure 4.5 (e)**). It is considered that the viscous flow coming from the irradiation cone carries the MPs to the outside. Moreover, the trapped MPs are always located inside the white "ring". The MP sometimes deforms the edge of the ring towards outside (**Figure 4.5 (e)**), which

facilitates its further expansion (**Figure 4.5 (f)**). Upon switching off the trapping laser, the "ring" shrinks quickly, but surprisingly the MP is remained at the same place.

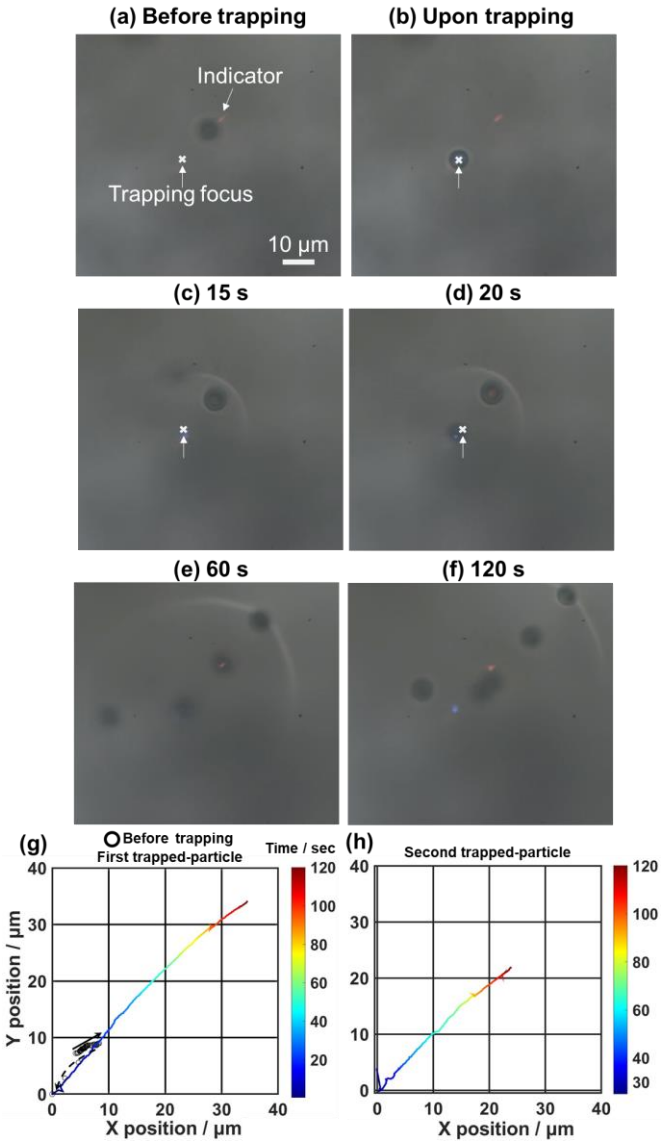

Figure 4.5 (a)-(f) Transmission images of moving polystyrene microparticles with the diameter of 6 μm at the surface of the 375 mg/mL lysozyme D_2O solution. The orange spot and white cross correspond to the reflection of the 640 nm monitoring and the focus of the 1064 nm trapping lasers, respectively. (g)-(h) Single particle tracking analyses of the first- and second-trapped microparticles.

4.4.3 Two-stage optical trapping dynamics

Based on the present results, we consider dynamics and mechanism of optical trapping and assembling phenomenon (**Figure 4.6**). In general, lysozyme proteins in solution can be found in dynamic equilibrium between monomeric and clustered structures [45,46]. It is theoretical demonstrated that more than 50% of lysozyme forms clusters, even at the 100 mg/mL solution. These protein clusters contain from 2 to 20 monomers, favoring the formation of bigger clusters at concentrated solutions (346 mg/mL). Moreover, the size of the 10-monomer cluster was estimated as a few nm [43], which is too small for trapping with 1 W tightly focused laser [47]. On the other hand, Tsuboi et al. reported that lysozyme association is induced by optical trapping in solution and the size of the formed cluster becomes 20 nm [48]. Here we consider that such clusters are formed inside the irradiation cone of the focused trapping laser and pumped up to the solution surface, expanding along the surface. As the solution surface adsorption layer of lysozyme exists before trapping [49], lysozyme molecules and clusters flowing out from the focal area may interact with the surface lysozyme, aligning and accumulating themselves. This increases the thickness of adsorption layer (**Figure 4.6 (a)-(c)**), which is coined here as the first stage of optical trapping of lysozyme. Such protein association from the surface into the solution is reported for sunflower oil [42], supporting our idea.

When the lysozyme concentration reaches a threshold around 300 mg/mL, the “ring” appears in the transmission image. Further irradiation results in the continued flow of clusters from the irradiation cone. Then, the adsorption layer increases its thickness and the lysozyme association and orientation may not be controlled anymore. Instead, the pumped-up lysozyme clusters penetrate the layer and expel the initial layer to the side (**Figure 4.6 (d)-(e)**), which is called as the second stage of the optical trapping. A border

between the initial layer and the invading clusters correspond to the white “ring”. When we use the 375 mg/mL solution, the surface layer is thick enough before trapping, so the white “ring” is observed soon after switching on the irradiation (As showing in the **section 3.1**). Namely, the second stage is started soon after excitation in this case, supporting our proposal on the mechanism.

The molecular and cluster orientation of the assembled lysozyme layer at the first stage is only determined by the initial arrangement of lysozyme at the surface. On the other hand, the orientation and alignment of the invading and expanding proteins have no relation with the adsorption layer, instead association and mutual interaction of the clusters are determined by high intensity irradiation of the 1064 nm laser at the focus. The pushed out and expanding clusters may keep their mutual geometrical configuration, reflecting the long-range interaction originated at the laser focus. Thus, the border between the surface layer and the assembly of pushed-out clusters is due to the difference of association and orientation of lysozyme clusters; surface-determined and laser irradiation-controlled manners. This claim is further supported by the lack of motion of the remaining PS MPs during the “ring” shrinking after switching off the trapping laser. The lysozyme clusters are not pulled back from the expanded peripheral to the cone through the focal area. The orientational arrangement of interacting clusters disappears as the long-range interaction due to the high intensity irradiation at the focus does not work anymore. We proposed such long-range interaction through hydrogen bonding network for optical trapping of 100 nm PS MPs which also expands up to a few ten micrometers [50].

One may consider that the present large assembly formation is due to liquid-liquid phase separation induced by optical trapping [51]. In general, the droplets formed by

chemical, physical, and mechanical stimulation are stable after the stimulation is stopped and the solute concentration in the droplet is homogeneous. Here, the assembly slowly disappears and the concentration has some gradient from the focus to the outside, which is inconsistent with conventional phase separation. Thus, the two-stage optical trapping will receive much attention and various applications will be opened.

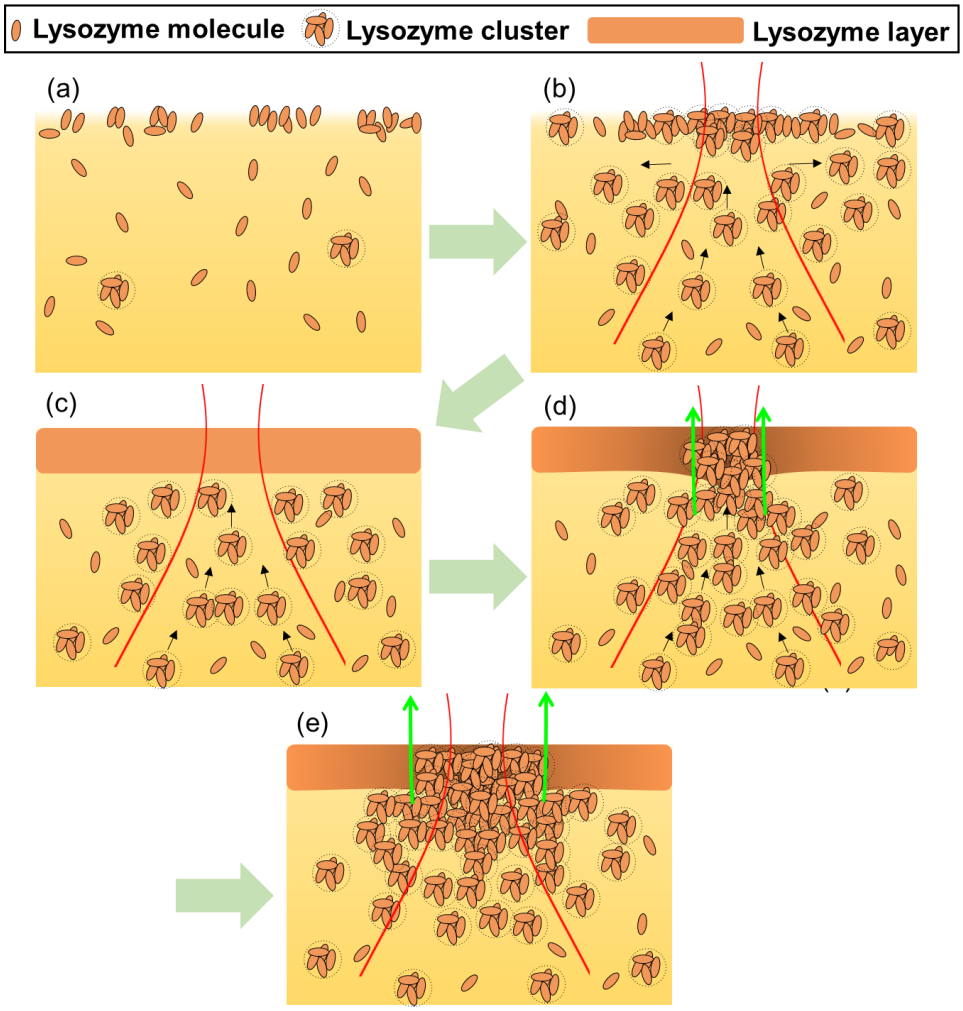

Figure 4.6 The illustrations showing two-stage optical trapping in the 200 mg/mL lysozyme solution where the 1064 nm laser is focused at the surface (red line). (b) to (c) correspond to the first stage optical trapping, and (d)-(e) represent the second stage. (a) Before trapping (~ 200 mg/mL), lysozyme is mostly dispersed as monomers and small clusters. (b) The assembling nonlinearly evolves with the irradiation time. (c) The surface layer of lysozyme with the

thickness of a few μm is prepared. (d) The assembled lysozyme clusters are pumped up and the surface layer is broken, allowing the pushed assembly to expand along the surface layer. The border between the surface layer and the assembly of pumped-up lysozyme clusters gives a white "ring" (green arrows). (e) The latter trapping is further developed.

4.5 Summary

In this synchronized experiment, fluorescence imaging and transmission imaging are performed simultaneously to examine the existence of the concentration gap. Surprisingly, the concentration distribution between inside and outside of the ring is in gradient, implying the formation of the ring induced by the other reason such as molecular orientation rather than the concentration difference. The trajectory of single PS MPs in lysozyme solution under trapping laser introduced enables the imitation of lysozyme cluster dynamics. Hence, we propose the two-stage optical trapping dynamics mechanisms for this unique optically evolved assembling behavior.

It is well known that lysozyme is abundantly distributed in nature and used as an antimicrobial enzyme (immune system), pharmaceutical drug, protective barrier of conjunctiva (eye), and food preservative [52]. Recently assembled liquid protein is considered to have biological function inside the living cells [53]. The present result will be developed as a spatiotemporal method for studying protein function in-vivo. The two-stage optical trapping has high potential in understanding protein assembling and developing its function.

Chapter 5 Mechanical property of lysozyme crystal

5.1 Introduction

Crystal engineering has been playing a vital role for elucidating functions of protein. Understanding of intermolecular interactions in the protein assembly is critical to its application [54]. The fundamental features of the crystal are determined by this interplay between the structure and properties of the molecule. For example, the chemical and physical properties (e.g. stability and solubility) vary in different crystal polymorphs [55,56]. Needless to say, the biological activity is also strongly connected to the protein packing, which is significantly integrated in its mechanical properties [57]. Given the circumstance, elucidating mechanical properties of the protein assembly is indispensable to facilitate protein engineering for materials development [58,59].

Young's modulus of the crystal is an essential parameter for investigation of its mechanical properties. The AFM indentation test has been widely applied for evaluating it in μm-scale elastic materials [60]. In this method, the AFM cantilever is contacted on the object to detect the indentation as a function of the force applied by the cantilever. The Young's modulus is evaluated based on Hertz contact theory [61]. This method allows mechanical property of isotropic material to be evaluated, but the simple indentation test is insufficient for anisotropic material like protein crystal. In addition, when the protein crystal swells with medium, its surface and interior may have different properties. Therefore, there is a demand for a more flexible evaluation method to evaluate the crystal elasticity at the specific part in several directions.

Our original measurement method, PLAIRE is match with this requirement [29,30,62]. In this method, an infrared femtosecond laser pulse is focused on or nearby a

micro-scale object into the aqueous solution under a microscope, as mentioned in **Section 1.4.1**. The laser irradiation induces an explosion at the laser focal point with highly efficient multiphoton absorption. The localized explosion around 1 μm generates a stress wave that propagates to the object. The wave vibration is detected by an AFM cantilever attached to the object. The cantilever is capable to detect vibrations in different directions in the crystal by controlling the laser focal point. Analyzing the vibration dependence expects flexible evaluation of mechanical properties of the protein crystal.

In this chapter, the work of applying the PLAIRE for observing elasticity of protein microcrystal for the first time demostration. The femtosecond laser pulse was directly focused on the crystal under microscope. The vibration due to the explosion propagated in and on the crystal and detected by an AFM cantilever attached to the crystal surface near the laser focal point. The Young's modulus of the crystal was evaluated from distance dependence between the laser focal point and contact point of the cantilever. We compared the modulus with it estimated from the conventional AFM indentation test (AFM force curve measurement) and discussed the difference between these values.

5.2 Atomic force microscope indentation measurement

The conventional force curve measurement was performed to acquire the Young's modulus to compare the results from the wave velocity estimation. **Figure 5.1 (i,ii)** illustrate the process of the cantilever approaching and retracting from the micro-lysozyme crystal respectively. The cantilever (qp-SCONT-10) with a spring constant of 0.01 N/m and a half cone angle of 25° was used. The piezo stage can precisely control the AFM cantilever in three dimensional and the signal from the deformation of the cantilever can be extracted in an nm scale. The relation between the compressing depth and the

exerting force from the sample is obtained by the force-distance curve mode of the AFM (Pacific Nano-technology, Nano-R2) as shown in **Figure 5.1 (iii)**. The data fitting was performed using JPK-SPM Date Processing software (JPK). The **green curve** represents the fitting curve using the Hertz-contact theory as the following equation:

$$F = \frac{2E(tan\alpha)d^2}{(1-v^2)\pi} \qquad (5.1)$$

where E is the Young's modulus of the lysozyme crystal to be determined by the fitting of the force-indentation curve, F is the loaded force on the micro-lysozyme crystal, ν is the Poisson's ratio, same as the Eq (1.), α is the half cone angle of the tip and d is the indentation depth. F and d were obtained from the force curve measurements [63]. As a result, the Young's modulus of lysozyme crystal is about 500 MPa with a 10% of deviation which is in good agreement with previous reports on the mechanical property of lysozyme crystal [58].

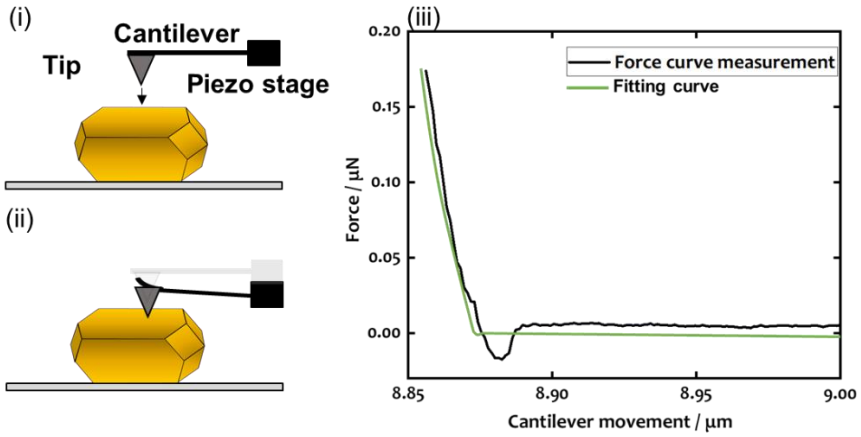

Figure 5.1 (i) Force curve measurement starts from the contact position followed by (ii) pushing down the sample and then going back to the initial position. (iii) Force curve of the lysozyme crystal and the Hertz fitting curve. Schematic illustration

5.3 Vibration waveform of surface elastic waves

5.3.1 Temporal vibration

We examine the dependence of the distance between the cantilever to the laser focal point in a systematic manner to investigate the elasticity of the micro-lysozyme crystal through the estimation of its Young's modulus. As shown in **Figure 5.2 (a)**, the temporal-vibration waveform was measured with the varied distance, 200, 400, and 600 μm. **Figure 5.2 (b)** shows the recorded vibration on the lysozyme crystal with distances corresponding to **Figure 5.2 (a)**. A sharp peak appears soon after the fs laser irradiation in each waveform (**Figure 5.2 (b))** is ascribed to the direct scattering of the fs laser beam to the photodiode in the AFM. As the sound velocity in lysozyme crystal is reported to be about 2000 m/s [64]; thus, the pressure wave-induced vibration may be arriving within the time region of scattered light so that is considered indistinguishable under the conditions used. Since the fs laser-induced impulse cannot propagate through the air, the peak in the temporal waveform is purely from the crystal vibration. Noteworthy, the arrival time of the subsequent peak indicates a correlation of the distance, suggesting the vibration is resulted from a single oscillation source with a constant velocity, as shown in **Figure 5.2 (b)** which is contained of the individual examination of three different micro-lysozyme crystals. We assumed this later-arriving wave was a surface acoustic wave, that is, a Rayleigh wave.

In order to visualize the arrival time of the Rayleigh wave accurately, the denoised process is stressed into the waveform (**Figure 5.3**). The arrival time, which was chosen at the time that amplitude started decreasing, on each waveform is about 2, 4, and 6 μs, pointed out by the arrow as shown, corresponding to the distance of 200, 400, and 600

μm. The amplitude of the temporal waveform indicates the surface vibration or deformation of lysozyme crystal directly detected by the motion of the AFM cantilever. As the crystal shape, volume, and weight are different in every measurement, the results of the amplitude fluctuate even with the same distance between the laser focal point and the AFM cantilever. Consequently, the amplitude is recognized as an irrelevance to our estimation of the mechanical property. We demonstrated that the PLAIRE technique enables us to identify the species from the Rayleigh wave velocity.

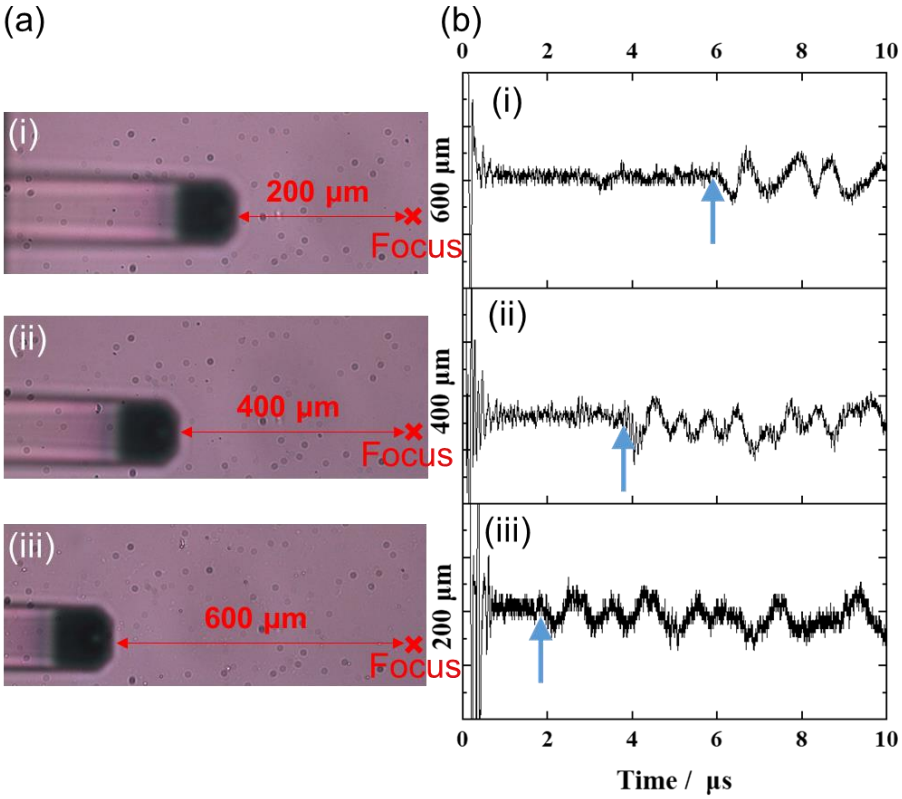

Figure 5.2 (a) Schematic of varied distance between the AFM cantilever and fs laser focal point. (i) – (iii) Distances are 200, 400, and 600 μm respectively. (b) Temporal profiles of elastic waves on the lysozyme crystal at a contact point of the AFM cantilever. (i) − (iii) Corresponding to (a)-(i) to (a)-(iii) and within a time range, of 3, 5, and 8 μs respectively. The blue arrow on each graph indicating the arrival time of elastic waves.

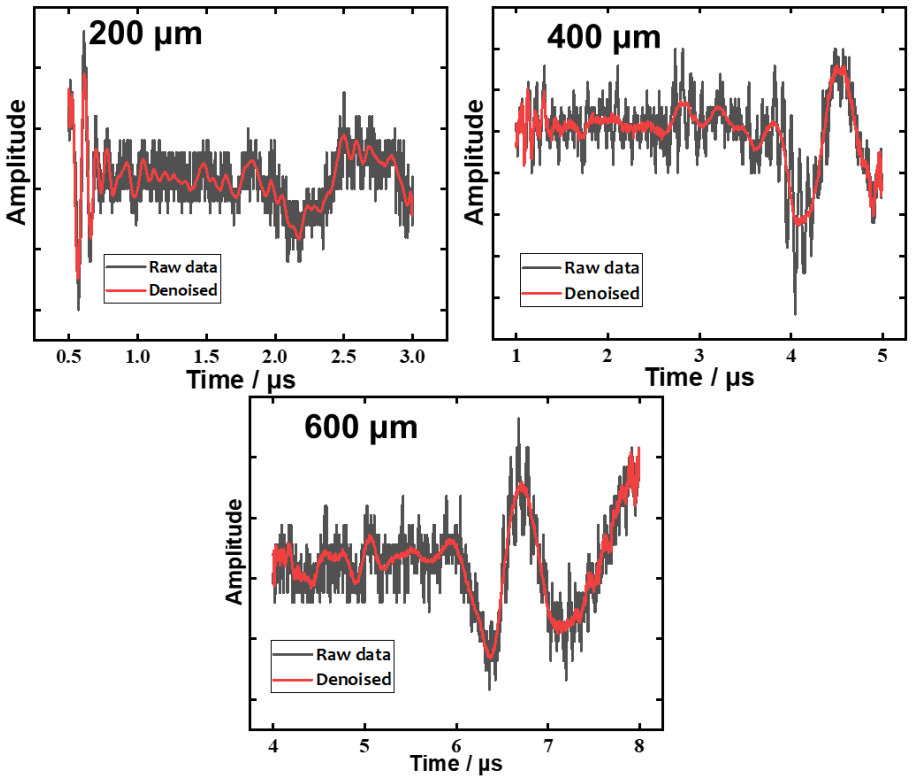

Figure 5.3 The denoised spectrum of the raw data of the temporal vibration waveform.

5.3.2 Frequency domain

The Fast Fourier Transform (FFT) was performed for obtaining the frequency domain which is converted from the time domain of the vibration waveform. Since the time domain vibration only provides the spatial information, on the on the other hand, the frequency domain is the classification of the periodic oscillation. If only one kind of period is in the time domain, i.e. the case of single direction-force, there will be only one peak appears in the frequency domain. In our PLAIRE experiment, it seems more complicated than the single force case, the time domain waveform resulted from the laser-ablation includes more kind of period of the oscillation. It is because the laser-ablation-induced vibration is excited from the isotropic impulse, which spreads from the ablation area to the outside and eventually is detected by the AFM cantilever. Even though only

one single pulsed laser shot may generate this complex vibration. Consequently, we take the advantage of frequency domain using FFT analysis to define our laser abalation induced vibration source. As shown in **Figure 5.4** there is no significant shift among the three different distances, indicating the temporal vibration waveforms are similar except for the arrival times and amplitudes are different.

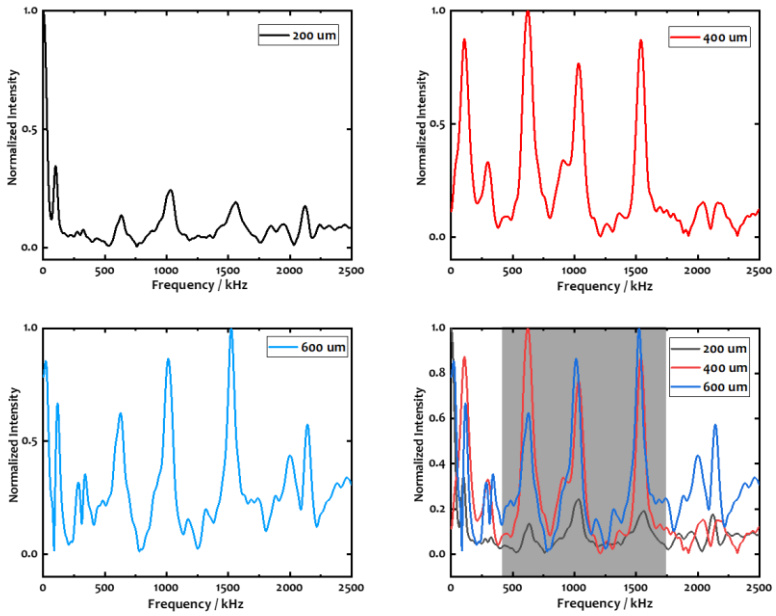

Figure 5.4 Frequency domain of each distance. Right lower: the overlaid of the frequency domain for all distances.

5.4 Discussion of Young's modulus difference

5.4.1 Estimation of surface elastic waves velocity

Figure 5.5 summarizes the results of the Young's modulus estimation from the Rayleigh wave velocity and the comparison between both methods. The relationship between the arrival times of Rayleigh waves and the varying distances from the laser focal point to the AFM cantilever is plotted in **Figure 5.5**. The propagation velocity of Rayleigh wave V_R was estimated to be about 108 m/s as a reciprocal of the slope in the plot by the linear fitting. In theory, (V_R) along the targeted sample can be described as a function of

its Young's modulus as follow:[65–67]

$$V_R = \sqrt{\frac{0.87E}{2\rho(1+\nu)}} \qquad (5.2)$$

where ρ is the lysozyme density with given values of 1350 kg/m^3, E is the Young's modulus of the lysozyme crystal to be determined by V_R, and ν is the Poisson's ratio (0.33 for lysozyme crystal)[68,69], as. By regarding the V_R value as 108 m/s and substituting it to **Eq. (1)**, the Young's modulus of lysozyme crystals was obtained. In **Figure 5.5 (b)**, the comparison is including both estimations from Rayleigh wave velocity and Hertz-contact theory **Eq. (2)** based on the force curve measurements. Surprisingly, Young's modulus estimation of V_R was about ten-fold small than the value from the force curve measurement. One potential reason is the moisture remaining on the microcrystal surface affects wave propagation. Rayleigh waves specifically propagate via the surface layer whereas the detected layer for force curve measurement may be much thicker than that of V_R estimation. We assume that the surface property is a crucial factor in Rayleigh wave propagation, thus the moisture is sensitive to the estimation comparably. However, in our sample preparation, the microcrystals were formed after the water evaporated completely which took about 7 days for waiting. Given the situation, we consider the moisture problem is a minor effect for our estimation.

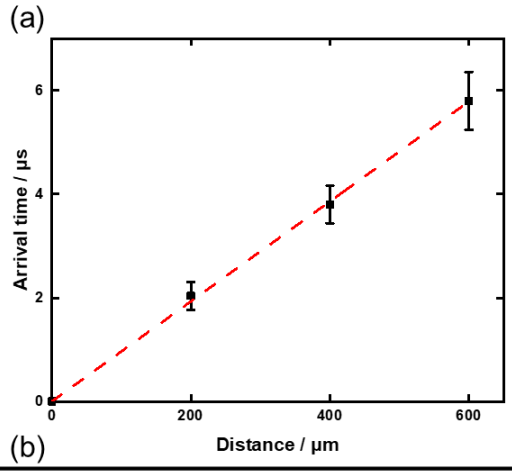

(b)

	Rayleigh wave	Hertz contact
Young's modulus	50 MPa	500 MPa

Figure 5.5 (a) The traveling distance between the AFM cantilever and laser focal point as the function of the Rayleigh wave arriving time. The red dotted line indicates the linear fitting. (b) Young's moduli of the lysozyme crystal measured by the force curve and by the propagating velocities of Rayleigh waves.

5.4.2 Advantage of the PLAIRE technique

As an alternative possible mechanism to explain the significant difference between the two estimations, we suggest that the in-plane and out-of-plane properties are essential to be taken into account. The lower value, 50 MPa, and the higher value, 500 MPa, are highly related to the in-plane and out-of-plane of the lysozyme crystal respectively. Crystals are structured in periodic alignment whose properties of thin films differ from the bulk, which can be described through the in-plane, and the out-of-plane, as they contain different numbers of the molecule in each aspect. We infer that the out-of-plane property dominates the average Young's modulus of the microcrystal, reflected by the force curve measurement, that is, AFM indentation method. In contrast, the in-plane property determines the thin film which may reflect the intrinsic mechanical property of

the crystal surface. As shown in **Figure 5.6**, the conventional AFM indentation method, exerting a direct perpendicular force to the crystal results in the lysozyme molecules extruding with each other longitudinally (left figure). For the Rayleigh wave detection method, the shock induced-impulse exerts parallel force along the crystal surface, exciting the collision of the lysozyme molecule with each other in a transverse manner attribute to the in-plane property, enabling the evaluation of surface stiffness. We conclude our PLAIRE technique has the potential to determine the lattice parameter of the microcrystal such as the in and out of plane property in this case, further to identify the isotropic and anisotropic property of the micro crystal.

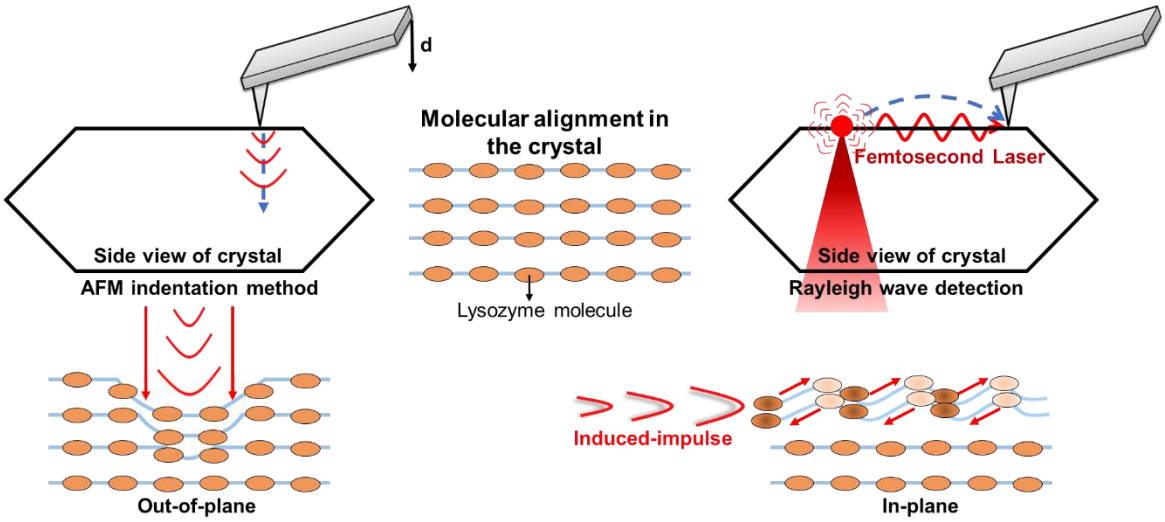

Figure 5.6 Comparison of AFM indentation method and Rayleigh wave detection method.

5.5 Summary

In conclusion, we applied a femtosecond-laser-induced impulsive force to the protein microcrystal directly without any additional assisted aqueous solution, as an exerted force to induce elastic waves. By taking the advantage of the sensitive detection from the AFM cantilever, we successfully detected the surface acoustic wave, the Rayleigh wave, propagating along the surface of the microcrystal. The results suggest that PLAIRE is a feasible technique to identify and analyze the elastic wave for the

microcrystal surface specifically. Of note, we propose a new method to evaluate the mechanical property of microprotein crystals from the differentiation of force curve measurement and V_R estimation depending on the out-of-plane and in-plane properties.

Our future work that will follow the present work to show the versatility of this PLARE technique. One idea is the spray coating of the crystal surface with various thicknesses of substances [70]. The systematic investigation may provide a new vision of our viewpoint in terms of the mechanical property. Furthermore, it is worth trying the solution samples which may enable us to estimate the viscosity and further upgrade the PLARE technique to a new horizon.

Chapter 6 Conclusion and Perspective

We succeeded in fabrication of lysozyme assembly by laser trapping at solution surface which is also considered as “optical evolved assembling”. Even only introduce one tiny focused laser beam at the solution surface, the assembly can still reach to submillimeter-size whose concentration can reach to about 4 times at the center of the laser focal area. Regard to the morphology of protein assembly, PS MPs was used for the indication, enabling us to statistically deduce its three-dimensional structure. Aside from the indicator role of PS MPs, the cooperative assembly is also a brand-new finding. This unique phenomenon due to the association between lysozyme and PS MPs was discovered and its dynamics, and the mechanism were uncovered by optical imaging and the microspectroscopy. As far as we know, no one has reported such preparation for this highly condensed protein assembly and this cooperative-trapping phenomenon before. This well-studied technique (optical trapping) make the breakthrough for protein assembly and condensation. We conclude that the current result will give us many possible ideas to fabricate large size materials characteristic of optical trapping especially on the hybrid-materials.

We proposed the two-stage optical trapping behavior by systematically investigate its formation on the response of laser power and initial concentration dependence. Apparently, in the case of lower initial concentration of lysozyme solution, there are two trends of temporal EF over trapping laser irradiation time. We discussed about the threshold concentration of lysozyme solution affecting the cluster size, interaction, surface adsorption and how it further changes the trapping behavior. Including the consideration of the trajectory of PS MPs in high concentration lysozyme solution while

laser trapping is turned on. The motion of the PS MPs is a valid imitation of the movement of the protein molecules/clusters, allowing us to gain the viewpoint in terms of molecular dynamic under optical force. Overall, the existence of the thick adsorption layer is in assistance of the molecular orientation. After the formation of the thick adsorption layer (threshold concertation), lysosome clusters are much larger and tend to penetrate the adsorption layer, perturbating the original orientation. On the other hand, the "white ring" was defined as the concentration gap intuitively without any verification at first stage. To realize this clarification, synchronized-captured imaging system plays a key role. As a result, the concentration is in a gradient distribution from the laser focal point (maximum) to outside, implying that this protein assembly is an unconventional phase separation which is only formed under optical force.

We also successfully applied fs-laser on the evaluation of the mechanical property of protein crystal to excite the elastic wave for the vibration of the crystal surface. The detection of the elastic wave method is available for more specific and localized region of the object such as the surface property. Since the velocity of the surface acoustic wave is the reflection of the stiffness of the object with limited thickness, enabling us to distinguish the complex structure objects.

In future, we envision that both techniques for micromanipulation could be integrated together to realize the detection of the mechanical property of a protein assembly prepared by optical trapping.

References

[1] C.M. Dobson, Semin. Cell Dev. Biol. 15 (2004) 3–16.

[2] G. Chiesa, S. Kiriakov, A.S. Khalil, BMC Biol. 18 (2020) 1–18.

[3] V.N. Uversky, A. V. Finkelstein, Biomolecules 9 (2019).

[4] G.B. Irvine, O.M. El-Agnaf, G.M. Shankar, D.M. Walsh, Mol. Med. 14 (2008) 451–464.

[5] D.M. Mitrea, R.W. Kriwacki, Cell Commun. Signal. 14 (2016) 1–20.

[6] Z.H. Harvey, Y. Chen, D.F. Jarosz, Mol. Cell 69 (2018) 195–202.

[7] A.A. Hyman, C.A. Weber, F. Jülicher, Annu. Rev. Cell Dev. Biol. 30 (2014) 39–58.

[8] C.M. Jakobson, D.F. Jarosz, Curr. Opin. Syst. Biol. 8 (2018) 16–24.

[9] S. Gopalakrishnan, J. Xu, F. Zhong, V.M. Rotello, Adv. Sustain. Syst. 5 (2021) 1–12.

[10] D.P. Kuruwita, X. Jiang, D. Darby, J.L. Sharp, A.M. Fraser, Food Control 112 (2020) 107153.

[11] L. Valentini, S. Bittolo Bon, N.M. Pugno, Nanomaterials 8 (2018).

[12] Y. Kimura, P.R. Bianco, (2006) 868–874.

[13] K.C. Neuman, E.A. Abbondanzieri, R. Landick, J. Gelles, S.M. Block, Cell 115 (2003) 437–447.

[14] C. Bradac, Adv. Opt. Mater. 6 (2018) 1–26.

[15] Y. Harada, T. Asakura, Opt. Commun. 124 (1996) 529–541.

[16] S.E.S. Spesyvtseva, K. Dholakia, ACS Photonics 3 (2016) 719–736.

[17] S.F. Wang, K.I. Yuyama, T. Sugiyama, H. Masuhara, J. Phys. Chem. C 120

(2016) 15578–15585.

[18] J.S. Lu, T. Kudo, B. Louis, R. Bresolí-Obach, I.G. Scheblykin, J. Hofkens, H. Masuhara, J. Phys. Chem. C (2020).

[19] K.I. Yuyama, J. George, K.G. Thomas, T. Sugiyama, H. Masuhara, Cryst. Growth Des. 16 (2016) 953–960.

[20] K.I. Yuyama, T. Sugiyama, H. Masuhara, J. Phys. Chem. Lett. 4 (2013) 2436–2440.

[21] D. Strickland, G. Mourou, Opt. Commun. 56 (1985) 219–221.

[22] H. Zhang, S.B. Lu, J. Zheng, J. Du, S.C. Wen, D.Y. Tang, K.P. Loh, Opt. Express 22 (2014) 7249.

[23] M.K. Bhuyan, A. Soleilhac, M. Somayaji, T.E. Itina, R. Antoine, R. Stoian, Sci. Rep. 8 (2018) 1–12.

[24] T. Kishimoto, K. Masui, W. Minoshima, C. Hosokawa, J. Photochem. Photobiol. C Photochem. Rev. 53 (2022) 100554.

[25] Y. Hosokawa, Jpn. J. Appl. Phys. 58 (2019).

[26] Y. Hosokawa, K. Watanabe, T. Asahi, H. Fukumura, H. Masuhara, Bull. Chem. Soc. Jpn. 72 (1999) 909–914.

[27] T. Iino, Y. Hosokawa, Appl. Phys. Express 3 (2010).

[28] S. Tsugawa, Y. Yamasaki, S. Horiguchi, T. Zhang, T. Muto, Y. Nakaso, K. Ito, R. Takebayashi, K. Okano, E. Akita, R. Yasukuni, T. Demura, T. Mimura, K. Kawaguchi, Y. Hosokawa, Sci. Rep. 12 (2022) 13044.

[29] R. Yasukuni, R. Fukushima, T. Iino, Y. Hosokawa, Appl. Phys. Express 10 (2017).

[30] R. Yasukuni, D. Minamino, T. Watanabe, S. Yamada, T. Iino, Y. Bessho, T.

Matsui, Y. Hosokawa, Appl. Phys. A Mater. Sci. Process. 124 (2018) 1–5.

[31] T. Wu, Q. Jiang, D. Wu, Y. Hu, S. Chen, T. Ding, X. Ye, D. Liu, J. Chen, Food Chem. 274 (2019) 698–709.

[32] S. Ito, T. Sugiyama, N. Toitani, G. Katayama, H. Miyasaka, J. Phys. Chem. B 111 (2007) 2365–2371.

[33] P. Retailleau, M. Riès-Kautt, A. Ducruix, Biophys. J. 73 (1997) 2156–2163.

[34] E.T.O. Measure, A. In, 267 (1952) 188–190.

[35] D. Joshi, D. Kumar, A.K. Maini, R.C. Sharma, Spectrochim. Acta - Part A Mol. Biomol. Spectrosc. 112 (2013) 446–456.

[36] C. V. Bindhu, S.S. Harilal, Anal. Sci. 17 (2001) 141–144.

[37] A. Kathiravan, V. Anbazhagan, M.A. Jhonsi, R. Renganathan, Zeitschrift Fur Phys. Chemie 221 (2007) 941–948.

[38] V. Kocherbitov, J. Latynis, A. Misiuì, J. Barauskas, G. Niaura, J. Phys. Chem. B 117 (2013) 4981–4992.

[39] R.A. Campbell, A. Tummino, I. Varga, O.Y. Milyaeva, M.M. Krycki, S.Y. Lin, V. Laux, M. Haertlein, V.T. Forsyth, B.A. Noskov, Langmuir 34 (2018) 5020–5029.

[40] L. Xing, K. Lin, X. Zhou, S. Liu, Y. Luo, J. Phys. Chem. B 120 (2016) 10660–10667.

[41] A. Diaspro, F. Federici, M. Robello, Appl. Opt. 41 (2002) 685–690.

[42] A. Poirier, A. Stocco, R. Kapel, M. In, L. Ramos, A. Banc, Langmuir 37 (2021) 2714–2727.

[43] A. Baumketner, W. Cai, Phys. Rev. E 98 (2018) 1–11.

[44] T. Visser, J. Oud, G. Brakenhoff, Optik (Stuttg). 90 (1992) 17–19.

[45] A. Stradner, H. Sedgwick, F. Cardinaux, W.C.K. Poon, S.U. Egelhaaf, P. Schurtenberger, Nature 432 (2004) 492–495.

[46] A. Shukla, E. Mylonas, E. Di Cola, S. Finet, P. Timmins, T. Narayanan, D.I. Svergun, Proc. Natl. Acad. Sci. U. S. A. 105 (2008) 5075–5080.

[47] D.S. Bradshaw, D.L. Andrews, Eur. J. Phys. 38 (2017).

[48] Y. Tsuboi, T. Shoji, M. Nishino, S. Masuda, K. Ishimori, N. Kitamura, Appl. Surf. Sci. 255 (2009) 9906–9908.

[49] Y.F. Yano, E. Arakawa, W. Voegeli, C. Kamezawa, T. Matsushita, J. Phys. Chem. B 122 (2018) 4662–4666.

[50] C.L. Wu, S.F. Wang, T. Kudo, K.I. Yuyama, T. Sugiyama, H. Masuhara, Langmuir 36 (2020) 14234–14242.

[51] F. Walton, K. Wynne, Nat. Chem. 10 (2018) 506–510.

[52] S.A. Ragland, A.K. Criss, PLoS Pathog. 13 (2017) 1–22.

[53] N. Nawaz, S. Wen, F. Wang, S. Nawaz, J. Raza, M. Iftikhar, M. Usman, (2022).

[54] G.R. Desiraju, J. Am. Chem. Soc. 135 (2013) 9952–9967.

[55] A.E. Nielsen, O. Sohnel, 11 (1971) 233–242.

[56] Y. Mori, M. Maruyama, Y. Takahashi, K. Ikeda, S. Fukukita, H.Y. Yoshikawa, S. Okada, H. Adachi, S. Sugiyama, K. Takano, S. Murakami, H. Matsumura, T. Inoue, M. Yoshimura, Y. Mori, Appl. Phys. Express 8 (2015) 1–5.

[57] S. Saha, M.K. Mishra, C.M. Reddy, G.R. Desiraju, Acc. Chem. Res. 51 (2018) 2957–2967.

[58] S. Tait, E.T. White, J.D. Litster, Part. Part. Syst. Charact. 25 (2008) 266–276.

[59] M. Rabiei, A. Palevicius, A. Dashti, S. Nasiri, A. Monshi, A. Vilkauskas, G. Janusas, Materials (Basel). 13 (2020) 1–17.

[60] M.F. Dupont, A. Elbourne, E. Mayes, K. Latham, Phys. Chem. Chem. Phys. 21 (2019) 20219–20224.

[61] O. Chaudhuri, S.H. Parekh, W.A. Lam, D.A. Fletcher, Nat. Methods 6 (2009) 383–387.

[62] R. Yasukuni, D. Minamino, T. Iino, T. Araki, K. Takao, S. Yamada, Y. Bessho, T. Matsui, Y. Hosokawa, Biomed. Opt. Express 12 (2021) 1366.

[63] Q.S. Li, G.Y.H. Lee, C.N. Ong, C.T. Lim, Biochem. Biophys. Res. Commun. 374 (2008) 609–613.

[64] S. Speziale, F. Jiang, C.L. Caylor, S. Kriminski, C.S. Zha, R.E. Thorne, T.S. Duffy, Biophys. J. 85 (2003) 3202–3213.

[65] Y. Yoshitake, S. Mitani, K. Sakai, K. Takagi, Phys. Rev. E - Stat. Nonlinear, Soft Matter Phys. 78 (2008) 1–7.

[66] M. Li, Z. Feng, Rev. Sci. Instrum. 87 (2016).

[67] P.G. Malischewsky, T.T. Tuan, J. Acoust. Soc. Am. 126 (2009) 2851–2853.

[68] S. Guo, B.B. Akhremitchev, Langmuir 24 (2008) 880–887.

[69] A.K.W. Leung, M.M.V. Park, D.W. Borhani, J. Appl. Crystallogr. 32 (1999) 1006–1009.

[70] C. Sanchez, C. Boissiere, S. Cassaignon, C. Chaneac, O. Durupthy, M. Faustini, D. Grosso, C. Laberty-Robert, L. Nicole, D. Portehault, F. Ribot, L. Rozes, C. Sassoye, Chem. Mater. 26 (2014) 221–238.

Achievements

Journal publications

1. **Po-Wei Yi**, Wei-Hsiang Chiu, Tetsuhiro Kudo, Teruki Sugiyama*, Roger Bresolí-Obach,* Johan Hofkens, Eri Chatani, Ryohei Yasukuni, Yoichiroh Hosokawa,* Shuichi Toyouchi,* and Hiroshi Masuhara. "Cooperative Optical Trapping of Polystyrene Microparticle and Protein Forming a Submillimeter Linear Assembly of Microparticle". *The Journal of Physical Chemistry C*, **2021**, 125 (34), 18988-18999
2. **Po-Wei Yi**, Wei Hsiang Chiu, Shuichi Toyouchi*, Roger Bresolí-Obach*, Johan Hofkens, Eri Chatani, Yoichiroh Hosokawa*, Teruki Sugiyama*, and Hiroshi Masuhara*. "Two-step optical trapping and assembling of protein at air/solution interface". *Applied Physics Express*, **2023**, 16, 025501
3. **Po-Wei Yi**, Kazuki Inoue, Tao Tang, Yuka Tsuri, Hiroshi Masuhara*, Teruki Sugiyama*, and Yoichiroh Hosokawa*. "Pulsed-laser-activated impulse response encoder (PLAIRE): Evaluation of surface elasticity on microprotein crystal". To be submitted to Applied Physics Express, **2023**

Related journal publications

1. Coherent Narrow-Band Light Source for Miniature Endoscopes. Zhan-Yu Chen, Ankur Gogoi, Shao-Yu Lee, Yuan Tsai-Lin, **Po-Wei Yi**, Ming-Kuan Lu, Chih-Cheng Hsieh, JinChang Ren, Stephen Marshall, and Fu-Jen Kao* . IEEE JOURNAL OF SELECTED TOPICS IN QUANTUM ELECTRONICS, 2019 VOL. 25, NO. 1, 7100707
2. Identification of Single Yeast Budding Using Impedance Cytometry with a Narrow

Electrode Span. Xun Liu, Tao Tang,* **Po-Wei Yi**, Yapeng Yuan, Cheng Lei, Ming Li, Yo Tanaka, Yoichiroh Hosokawa, and Yaxiaer Yalikun*. Sensors 2022, 22, 7743

Conference

1. **The 83rd JSAP Autumn Meeting (Japan Society of Applied Physics) 2022**

   Po-Wei Yi, Yuka Tsuri, Kazuki Inoue, Teruki Sugiyama, Hiroshi Masuhara, Yoichiroh Hosokawa (Oral presentation) "*AFM Detection of Vibration Propagation in a Protein Microcrystal Triggered by Femtosecond Laser Impulse"*

2. **The Japanese Photochemistry Association Annual Meeting 2022**

   MASUHARA Hiroshi, **YI Po-Wei**, TOYOUCHI Shuichi, CHIU Wei-Hsiang, BRESOLÍ-OBACH Roger, HOFKENS Johan, CHATANI Eri, YASUKUNI Ryohei, HOSOKAWA Yoichiroh, SUGIYAMA Teruki (Oral presentation) *"Fluorescence Imaging and Raman Spectral Analyses of Optically Evolved Assembling of Lysozyme at Air/Solution Interface"*

3. **The 82nd JSAP Autumn Meeting (Japan Society of Applied Physics) 2021**

   Po-Wei. Yi, Wei-Hsiang Chiu, Tetsuhiro Kudo, Roger Bresolí-Obach, Johan Hofkens, Eri Chatani, Ryohei Yasukuni, Yoichiroh Hosokawa, Teruki Sugiyama, Shuichi Toyouchi, Hiroshi Masuhara (Oral presentation) *"Optically Evolved Condensation of Lysozyme Study by Raman Microspectroscopy"*

4. **The 68th JSAP Spring Meeting (Japan Society of Applied Physics) 2021**

   Po-Wei. Yi, Wei-Hsiang Chiu, Tetsuhiro Kudo, Roger Bresolí-Obach, Johan Hofkens, Eri Chatani, Ryohei Yasukuni, Yoichiroh Hosokawa, Teruki Sugiyama, Shuichi Toyouchi, Hiroshi Masuhara (Oral presentation) *"Single Sub-Millimeter Linear Assembly of Polystyrene Microparticlesby Optical Trapping at Protein Solution*

Surface"

5. **International Conference on Photochemistry 2021**

   Po-Wei Yi, Wei-Hisang Chiu, Tetsuhiro Kudo, Roger Bresolí-Obach, Johan Hofkens, Eri Chatani, Ryohei Yasukuni, Yoichiroh Hosokawa, Teruki Sugiyama, Shuichi Toyouchi, Hiroshi Masuhara (Oral presentation) *"Optical force-induced three-dimensional protein assembly growing from solution surface"*

6. **The Japanese Photochemistry Association Annual Meeting 2021**

   TOYOUCHI Shuichi, **YI Po-Wei**, CHIU Wei-Hsiang, BRESOLÍ-OBACH, Roger, HOFKENS Johan, CHATANI Eri, SUGIYAMA Teruki, YASUKUNI Ryohei, HOSOKAWA Yoichiroh, MASUHARA Hiroshi (Oral presentation) *"Optically evolving condensation of protein: A sub-millimeter 3-dimensional domain formation from solution surface"*

7. **The 81st JSAP Autumn Meeting (Japan Society of Applied Physics)**

   Po-Wei Yi, Tetsuhiro Kudo, Eri Chatani, Ryohei Yasukuni, Yoichiroh Hosokawa, Teruki Sugiyama, Hiroshi Masuhara (Oral presentation) *"Optical Trapping and Assembling of Protein at Solution Surface"*

Acknowledgements

First of all, I would like to express my sincere gratitude to my advisor Masuhara Hiroshi sensei (NYCU) for everything since the day I walked into his office. He firstly welcomed me to join his group without hesitation regardless of that I have zero experience on optical trapping. During the period of my PhD, he always teaches and discusses with me broadmindedly and patiently. Some of his words still ring my ears, “one time one parameter” or “I agree with you but I still like to debate with you”. I sincerely appreciate Masuhara sensei’s enthusiasm for research and education which affects me profoundly.

Deep down, I am certainly grateful to Hosokawa Yoichiroh sensei (NAIST). He is the person who proposed the idea of double degree to me at the very beginning. From then till now, no matter how busy Hosokawa sensei is, he always manages to make the time for me and help me out (both on science and daily life) when I am in need.

I would also like to give Sugiyama Teruki sensei (NYCU) my deep thanks. He always reminds me some important information before I aware such as the regulation of double degree and the entry of Japan. Sugiyama sensei also kindly gives his hand to me for troubleshooting of my experiment and answers my questions thoroughly until I fully understand.

I would also like to thank Yaxiaer Yalukun sensei (NAIST). In this short year, he is generous to provide me with some experiment ideas and the opportunity of career development. His share of experience based on the foreigner viewpoint really broadens

my vision.

I would also like to thank Ohta Jun sensei (NAIST) and Toma-Fukai Sachiko sensei (NAIST) for being my co-supervisors. In this year, they caught up my research plan quickly without omission and gave the great suggestions and questions that inspired me what should be modified in my research plan.

I would also like to thank Toyouchi Shuichi sensei (NYCU→OMU) and Kudo Tetsuhiro sensei (NYCU→TTI). They were my mentor when I was in NYCU. Under their guidance, I sincerely learned a lot from them. For example, how to do the experiment in a reliable way, how to treat the data in a convincing way, how to present our work clearly in English and how to make our story more attractive but still logical. Besides, Toyouchi sensei is an expert on spectroscopy and he also opened my interest in it.

I would also like to thank Johan Hofkens (KUL) for his kindness, welcoming me to his lab for short-term research. Specially thanks give to Roger Bresolí-Obach (KUL) for giving me the best care and teaching me a lot about science, and listening to my confusion, when I was in Leuven. I would not have such great memories without his company.

I would also like to thank Yasukuni Ryohei sensei (NAIST→OIT) for advising me and giving practical suggestions no matter where I am. Great advice always led me out of the hard time.

I would also like to thank to Cindy san and Sugiyama Chie san (secretaries in NYCU) and Tada Keiko san and Akita Eri san (secretary and assistant in NAIST) for helping me deal with all the massive paper works. Because of them, our group can work smoothly.

I would like to thank all the staffs and students of Laser Bio/Nano Laboratory and Bio-process Laboratory in NCTU and NAIST. The times shared with them will always be my precious memories of life

Finally, I would like to deeply express my gratitude to my family, my parents and my elder sister. Without their understandings and supports, it is difficult for me to decide to enter the PhD course and also to continue it until now. No matter how cruel it is out of there, I realize that my home is always my security blanket. Now, I completed this PhD journey and it about time to start the next chapter!